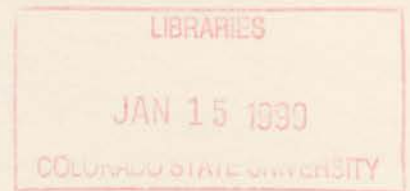


QC
852
.C6
No. 669
ATMOS

**LARGE PARTICLE CHARACTERISTICS OVER THE
SOUTHERN OCEAN DURING ACE 1**

By

**Janel T. Davis
and
Sonia M. Kreidenweis**



Funding Agency:

National Science Foundation (NSF), Significant Opportunities in Atmospheric
Research and Science (SOARS)
Colorado State University

**Colorado
State
University**

**DEPARTMENT OF
ATMOSPHERIC SCIENCE**

PAPER NO. 669

LARGE PARTICLE CHARACTERISTICS OVER THE SOUTHERN OCEAN
DURING ACE 1

by

Janel T. Davis

and

Sonia M. Kreidenweis

Department of Atmospheric Science

Colorado State University

Fort Collins, CO

NSF

under the Significant Opportunities in Atmospheric Research and Science (SOARS)

Colorado State University

December, 1998

Atmospheric Science Paper No. 669



U18401 6518639

47 129COL 2533
04/99 XL1
38-000-01 GEC

ABSTRACT
LARGE PARTICLE CHARACTERISTICS OVER THE SOUTHERN OCEAN
DURING ACE 1

The Aerosol Characterization Experiment (ACE-1) in November and December 1995 was designed to characterize aerosol physical, chemical and optical properties in remote marine regions in the Southern Hemisphere. Data from six ACE-1 research flights were used to examine concentrations of large particles in two size ranges: those having diameters, D_p , $0.5 \leq D_p \leq 50 \mu\text{m}$ (N_1) and those with $2.0 \leq D_p \leq 50 \mu\text{m}$ (N_2).

Reported here are observations of vertical profiles of N_1 and N_2 for heights, z , from ~ 30 to 7000 m over the ocean surface. Number concentrations near the surface ($z \leq 900$ m) varied from 0.8 to $\sim 30 \text{ cm}^{-3}$, while maximum N_2 concentrations were $\sim 2.0 \text{ cm}^{-3}$. Above altitudes of 2400 m, N_1 concentrations were found to vary from greater than 0.07 to 1.2 cm^{-3} . Significant concentrations ($> 0.02 \text{ cm}^{-3}$) of N_2 particles aloft were usually associated with regions of deep convection, cloud outflow, and cloud dissipation.

Calculated dry mass concentrations for N_1 particles near the surface ($z \leq 100$ m) assumed to be primarily sea salt, showed dependence on wind speed. Computed dry sea salt mass concentrations varied from 2.0 to $30.0 \mu\text{g m}^{-3}$ and varied with wind speed similarly to previously proposed relationships. Aerosol size distributions were used to compute particle light scattering coefficients and aerosol visible optical depths. The light scattering coefficient for N_1 particles ranged from 0.002 to 0.08 km^{-1} at altitudes less than

QC
852
.C6

no. 669
ATMOS

900 m, and from 0.00005 to 0.05 km⁻¹ at higher altitudes. For N₂ particles, the light scattering coefficient ranged from 0.001 to 0.05 km⁻¹ for z < 900 m and from 0.0003 to 0.04 km⁻¹ for z > 900 m. The large particles are a significant contribution to the total aerosol light scattering coefficient. Optical depths for these particles ranged from 0.043 to 0.085 for N₁ and from 0.019 to 0.039 for N₂.

ACKNOWLEDGMENTS

I would like to thank my advisor, Dr. Sonia Kreidenweis for her guidance and direction in my research during my stay at Colorado State University (CSU). She has provided me with many opportunities and experience in aerosol research. I would like to express my appreciation to Dr. Jeffrey Collett and Dr. David Dandy for valuable ideas they shared.

I would also like to thank Dr. Darrel Baumgardner for allowing me to use the ACE-1 data sets and contributing his time in providing useful information. I am appreciative to the Significant Opportunities in Atmospheric Research and Science (SOARS) for funding my research studies at CSU; without SOARS, I would not have had the opportunity of exploring atmospheric science. Dr. Thomas Windham also provided mentoring on various topics.

There are several people who gave me insight in developing codes and graphs for this research. Mrs. Debra Harrington and Dr. Fred Brechtel provided codes and graphs from IDL. Ms. Jenny Hand was helpful by explaining thesis preparation and the MIE scattering code. I am grateful to my husband for his patience and inspiration. He sacrificed his career to be with me as I finished my research. I would also thank Bethel Baptist Church for being a great support group. And finally, I give praises to my Lord and Savior, Jesus Christ for hearing my prayers and providing guidance through His word.

TABLE OF CONTENTS

ABSTRACT	ii
ACKNOWLEDGMENTS	iv
TABLE OF CONTENTS	v
LIST OF TABLES	vii
LIST OF FIGURES	viii
CHAPTER 1. INTRODUCTION	1
1.1 Experimental Background	4
CHAPTER 2. INSTRUMENTATION	7
CHAPTER 3. DATA SET	16
3.1 Removal of in-cloud data	16
3.2 Number concentration processing	16
3.3 Estimated lower detection limit	17
3.4 Determination of aerosol refractive index	18
3.5 Optical properties	22
CHAPTER 4. FSSP RESULTS	25
4.1 Vertical profiles of number concentrations	25
4.2 Number size distributions from the FSSP-300 and FSSP-100	30
4.3 Sea salt mass concentrations	32
4.4 Scattering properties	32
CHAPTER 5. DISCUSSION	53
5.1 Particle lifetimes	53
5.2 Effects of assumptions regarding aerosol water content	55
CHAPTER 6. SUMMARY AND CONCLUSIONS	59
CHAPTER 7. FUTURE WORK	61
REFERENCES	63

APPENDIX

ii		67
vi	A. Forward Scattering Spectrometer Probe (FSSP) model studies.....	67
v	A.1. Principle of operation of the FSSPs.....	68
iv	A.2. Sizing Calibrations	69
iii	A.3. Flow distortions.....	71
	A.4. Concentration corrections	72
i	A.5. Concentration and sizing uncertainties.....	72
4	A.6. Lower Detection Limit (LDL) approximations.....	73
CHAPTER 2 INSTRUMENTATION		
7		
CHAPTER 3 DATA SET		
16	3.1 Removal of in-cloud data	
16	3.2 Number concentration processing	
16	3.3 Estimated lower detection limit	
17	3.4 Determination of aerosol refractive index	
18	3.5 Optical properties	
CHAPTER 4 FSSP RESULTS		
25	4.1 Vertical profiles of number concentrations	
25	4.2 Number size distributions from the FSSP-300 and FSSP-100	
30	4.3 Sea salt mass concentrations	
32	4.4 Scattering properties	
CHAPTER 5 DISCUSSION		
23	5.1 Particle lifetimes	
23	5.2 Effects of assumptions regarding aerosol water content	
CHAPTER 6 SUMMARY AND CONCLUSIONS		
30		
CHAPTER 7 FUTURE WORK		
61		
REFERENCES		
63		

LIST OF FIGURES

LIST OF TABLES

CHAPTER 1 2

1.1.1 ACE-1 Scientific missions 6

CHAPTER 2 12

2.1 Instrumentation Accuracy 11

2.2 FSSP-300 midpoints for each bin as a function of refractive index 14

2.3 FSSP-100 midpoints for each bin as a function of refractive index 15

CHAPTER 3 32

3.4.1 Seawater Polynomial Coefficients 24

CHAPTER 4 32

4.1.1 Mean number concentrations and standard deviations 42

4.1.2 Mean surface area concentrations and standard deviations 43

4.1.3 Mean volume concentrations and standard deviations 44

4.3.1 Mean dry sea salt mass concentrations and standard deviations 49

4.4.1 Contribution of aerosol research to optical properties 51

4.4.2 Optical depth values for N_1 and N_2 52

4.2.1 Vertical profiles of temperature 45

4.2.2 Size distributions for the Boundary Layer 46

4.2.3 Size distributions for the Mid Troposphere 47

4.2.4 Size distributions for the Free Troposphere 48

4.3.1 Dry sea salt mass concentrations 49

4.4.1 Backscattering coefficient ($0.3 < D_p < 50$ microns and $2.0 > D_p > 50$ microns) 50

5.1.1 EM_1 as a function of relative humidity 53

5.2.1 Diffusional growth of individual drops 54

LIST OF FIGURES

CHAPTER 1	
1.1.1 Flight tracks.....	5
CHAPTER 2	
2.1 Size distributions for the Boundary Layer.....	12
2.1 Scattering Cross Section.....	13
CHAPTER 3	
3.2.1 N_{100} and N_2 time line.....	23
3.4.1 Hygroscopicity curve for NaCl and sea salt particles.....	24
CHAPTER 4	
4.1.1 Cloud number concentrations as a function of altitude.....	35
4.1.2 N_1 concentrations ($0.5 \leq D_p \leq 50 \mu\text{m}$).....	36
4.1.3 ΣN_1 as a function of altitude.....	37
4.1.4 N_2 concentrations ($2.0 \leq D_p \leq 50 \mu\text{m}$).....	38
4.1.5 ΣN_2 as a function of altitude.....	39
4.1.6 Vertical profiles of wind speed.....	40
4.1.7 ΣN_1 and ΣN_2 as a function of wind speed.....	41
4.2.1 Vertical profiles of temperature.....	45
4.2.2 Size distributions for the Boundary Layer.....	46
4.2.3 Size distributions for the Mid Troposphere.....	47
4.2.4 Size distributions for the Free Troposphere.....	48
4.3.1 Dry sea salt mass concentrations.....	49
4.4.1 Backscattering coefficient ($0.5 < D_p < 50$ microns and $2.0 < D_p < 50$ microns).	50
5.1.1 ΣN_2 as a function of relative humidity.....	57
5.2.1 Diffusional growth of individual drops.....	58

TABLE IN APPENDIX

APPENDIX A

	APPENDIX A	
A1.2.1	FSSP-100 Calibration	77
A1.1.2	Schematic of FSSP-100	
A1.2.1	Theoretical Response for refractive indices ranging from 1.38 - 1.48	
A1.2.2	Theoretical Response for refractive indices ranging from 1.48 - 1.58	
A1.0.1	Low number concentrations (N_1) for L&L approximation	

FIGURES IN APPENDIX

APPENDIX A

A1.1.1 Schematic of FSSP-100	74
A1.1.2 Schematic of FSSP-300	74
A1.2.1 Theoretical Response for refractive indices ranging from 1.36 – 1.46.....	75
A1.2.2 Theoretical Response for refractive indices ranging from 1.48 – 1.56.....	76
A1.6.1 Low number concentrations (N_l) for <i>LDL</i> approximation.....	77

CHAPTER 1. INTRODUCTION

Aerosols play direct and indirect roles in the Earth's climate by scattering and absorbing incoming and reflected short-wave radiation, and by influencing the formation and microphysics of clouds (Hegg *et al.*, 1996; Quinn *et al.*, 1995). Studies of the climate effects of aerosols have been largely focused on accumulation mode particles (diameters between about 0.1 and 1 μm), since these are the most likely to be influenced by anthropogenic activities; however, particles larger than 1 μm have also been shown to contribute significantly to scattering and absorption within the visible wavelengths (Quinn *et al.*, 1998). Supermicron particles also affect cloud microphysical properties, including possible drizzle enhancement by accelerating rates of collision / coalescence (Feingold *et al.*, 1998). Therefore, the vertical distributions and magnitudes of large particle number concentrations and size distributions are of interest, particularly in marine regions where cloud microphysical properties may be most susceptible to modification (Twomey, 1991).

In this work, we present vertical profiles of number concentrations and size distributions, estimated sea salt mass concentrations as functions of wind speed, scattering properties, and calculated optical depths for two categories of large particles: those with diameters, D_p , larger than 0.5 μm , and those with $D_p > 2.0 \mu\text{m}$. The data used are from research flights in the First Aerosol Characterization Experiment (ACE-1), conducted in November and December 1995 over the Southern Ocean. A specific goal of

ACE-1 was the characterization of the chemical, physical and radiative properties of aerosols in a remote marine environment. The research flights examined here were based in Hobart, Tasmania, a mid-latitude Southern Hemispheric marine site. Further details of the experiment can be found in Bates *et al.* (1998).

Previous work on the vertical distribution of large particles in marine regions includes that reported by Kristament *et al.* (1993), who studied aerosol properties in the remote marine regions of New Zealand and the Southwest Pacific. The data were obtained from flights by the Fokker F27 Friendship over a period of three years. Measurements from an active scattering aerosol spectrometer probe (ASASP 100X) and forward scattering spectrometer probe (FSSP 100) were used to develop best-fit equations for the vertical distribution of number concentration of accumulation ($0.12 \mu\text{m} \leq D_p \leq 0.5 \mu\text{m}$) and coarse mode ($D_p \geq 0.5 \mu\text{m}$) particles. The data were corrected back to standard temperature and pressure. The coarse mode aerosol concentrations were found to decrease exponentially with height to ~ 2400 m, and were negligible at higher altitudes, although there was a large standard deviation in the data. Conditions which may favor higher coarse mode number concentrations aloft are a particular focus of our work.

Measurements of coarse mode aerosol concentrations at the surface were made aboard the NOAA RV *Discoverer* during ACE-1 by Quinn *et al.* (1998). The instrumentation used for sampling was a seven-stage multi-jet cascade impactor (sampling air at 30 to 45% RH), with aerodynamic cutoff diameters of 0.27, 0.37, 0.64, 1.2, 2.3, 4.7, and $12 \mu\text{m}$. Quinn *et al.* (1998) found that sea salt accounted for $80 \pm 10\%$ of aerosol mass for $D_p < 1.0 \mu\text{m}$, and $99 \pm 0.7\%$ for $D_p > 1.0 \mu\text{m}$, confirming that sea salt is the major component of marine particle mass for coarse particles, and probably for

sizes as small as $0.5 \mu\text{m}$ (Murphy *et al.*, 1998). Correlations between the submicron sea salt mass concentration and local wind speed resulted in a coefficient of determination, r^2 , of 0.42, and those between the supermicron sea salt and local wind speed yielded $r^2 = 0.41$, indicating that about 40% of the variance in the sea salt mass concentration can be explained by local wind speed. Other factors that could affect the dependence of sea salt mass concentrations on wind speed are advection and vertical mixing (Quinn *et al.*, 1998; Gong *et al.*, 1997). These findings are of interest to the present study, since vertical mixing may also impact the number concentrations of large particles at higher altitudes.

Total sea salt aerosol mass concentrations in the study by Quinn *et al.* (1998) ranged from 3 to $25 \mu\text{g m}^{-3}$. In earlier work, Fitzgerald (1991) compiled observations from various experiments of background aerosols in the boundary layer over the remote oceans, and reported two correlations between sea salt mass concentrations and wind speed. The correlation determined from the data of Lovett (1978) used measurements from North Atlantic weather ships during 11 voyages from September 1974 to July 1975. Total sea-salt concentrations were measured by sampling through membrane filters at heights of 5, 10, and 15 m above sea level (ASL). Sea-salt concentrations ranged from 2.7 to $35.0 \mu\text{g m}^{-3}$ for winds less than 10 m s^{-1} . The second correlation was for the data of Gras and Ayers (1983), who reported measurements from the Australian baseline station site on the isolated headland of Cape Grim, Tasmania at an altitude of 94 m ASL. Two round jet impactors were used to collect particles with radii $0.025 \leq r \leq 0.5 \mu\text{m}$. Sea salt comprised $> 95\%$ of the total volume in this size range and varied from 2.0 to $20 \mu\text{g m}^{-3}$ for wind speeds less than 10 m s^{-1} . In the present study, data from low-level flight legs are used to estimate the volume (and hence mass) concentrations of coarse particles,

assumed to be sea salt, for comparison with those derived from more direct sampling methodologies. We also extend these estimates of sea salt mass concentrations to higher altitudes, and use them to estimate the contributions of sea salt to total aerosol optical depth.

Section 1.1. Experimental Background

Approximately 33 research flights were flown during ACE-1, with 162 flight hours originating from Hobart, Tasmania, between November 15 and December 14, 1995 during the spring and early summer period of the Southern Hemisphere (Bates *et al.*, 1998). Data from six flights occurring on November 18, 19, 24, 25, 28, and December 12 (research flights 11, 12, 14, 15, 17, and 28) were analyzed for this study, selected because of the range of conditions that they represent. These conditions include one flight that was geared toward sampling clear sky regions, and other flights, which studied cloud events. Figure 1.1.1 shows the flight tracks of each of the research flights (RF), and Table 1.1.1 summarizes the primary scientific missions addressed in each. Each flight began at approximately 22:50 UTC and returned after approximately 8 hours. RF 11 and 12 were flown southeast from the island, while RF 14, 15, 17, and 28 were flown in the vicinity of Tasmania. Vertical profiles of wind direction indicated that the sampled air was generally arriving from a clean marine sector, although the local wind direction cannot address transport occurring over larger spatial areas. Times of possible continental influence, identification of convective outflow regions, and other observations of interest to this work have been obtained from the observer notes found at <http://saga.pmel.noaa.gov/ace1.html>.

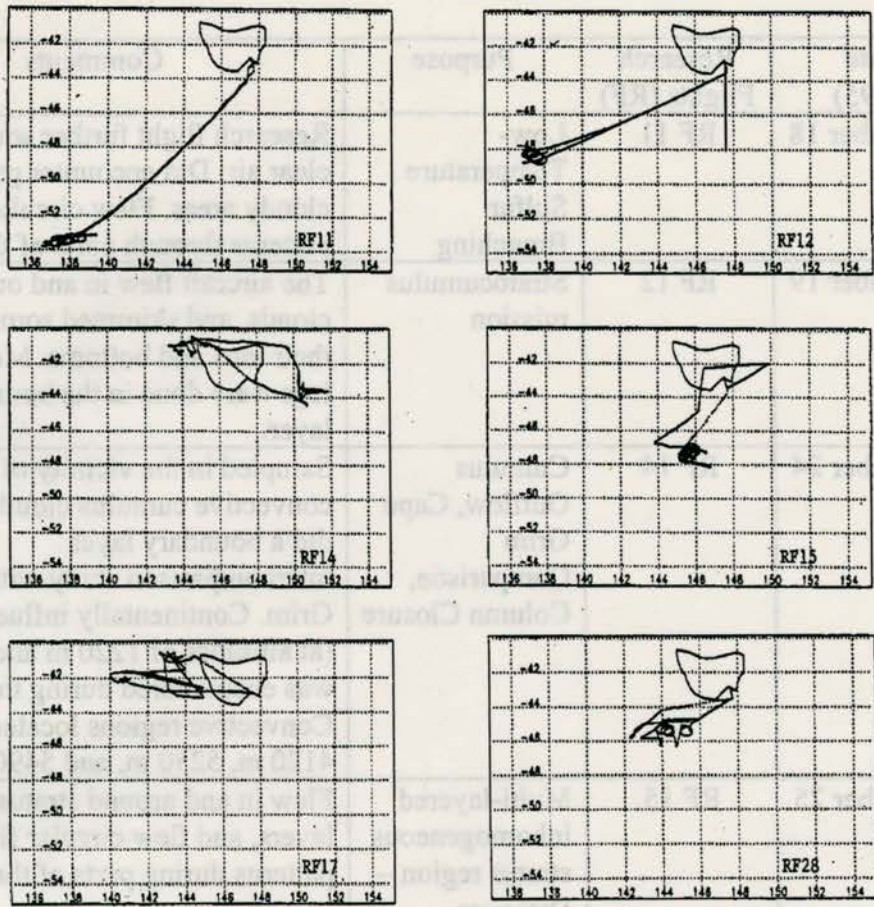


Figure 1.1.1 Flight tracks for a) RF 11, b) RF 12, c) RF 14, d) RF 15, e) RF 17, and f) RF 28. The x-axis is latitude, and the y-axis is longitude. Each flight began at Hobart, Tasmania. This island is located just below Australia.

Table 1.1.1 ACE-1 Scientific Missions.

Date (1995)	Research Flights (RF)	Purpose	Comments
November 18	RF 11	Low-Temperature Sulfur Branching	Research flight further south to find clear air. Did encounter partially cloudy areas. Flew circular flight patterns through parts of the flight
November 19	RF 12	Stratocumulus mission	The aircraft flew in and out of clouds, and skimmed some clouds at their tops and bottoms. Most flight legs were done in the boundary layer.
November 24	RF 14	Cumulus Outflow, Cape Grim Comparison, Column Closure	Sampled in the vicinity of convective cumulus clouds and also did a boundary layer intercomparison study with Cape Grim. Continentally influenced air (at altitudes of 1220 m and 1830 m) was encountered during the mission. Convective regions located around 4120 m, 5250 m, and 5490 m.
November 25	RF 15	Multi-layered inhomogeneous stratus region – Discover Intercomparison	Flew in and around stratus cloud layers, and flew circular flight patterns during parts of the flight.
November 28	RF 17	Cumulus Cloud – Particle Production	Explored theory that free troposphere may be source region of new particle production and whether this production is associated with cloud processes. Flew in and around deep, widespread cumulus towers to encounter clear outflow regions. Well-developed anvils located around 5900 m. Cloud outflow regions located at 2750 m.
December 12	RF 28	Stratocumulus – Radiation, Ship Flux Intercomparison	Aircraft flew in and out of cloud. Studied stratocumuli for drop characteristics. Encountered drizzle within the boundary layer.

CHAPTER 2. INSTRUMENTATION

The data used in this work were taken aboard the C-130 aircraft, owned by the National Science Foundation and operated by the National Center for Atmospheric Research (NCAR) Research Aviation Facility (RAF). The Honeywell (Model HG1095-AC03) Laseref SM Inertial Reference System and Trimble (TANS III) Global Positioning System (GPS) were used to determine aircraft position. The velocity was determined with a Rosemount pitot dynamic pressure probe. The Rosemount (Model 1501) Digital Pressure Transducer - Fuselage Port (PSFD) was used to determine ambient pressures. Altitudes were derived from static pressure measurements corrected for local altimeter settings. Rosemount (Model 510BF) Amplifier sensors were used to determine ambient temperatures. A General Eastern, Model 1011B Dew Point Hygrometer was used to derive relative humidity and dew point temperatures. Aerosol data were obtained from the Forward Scattering Spectrometer Probe Models 100 and 300 (FSSP-100 and FSSP-300). These sensors were mounted on the right wing pods of the aircraft and were within a meter of one another. A list of the accuracy of most instrumentation used in this study is shown in Table 2.1 (Baumgardner and Clarke, 1998). The numbers in brackets represent relative accuracies, which emphasize changes in quantities rather than their absolute magnitude.

The FSSP models 100 and 300 sample particles by collecting light scattered by individual particles that pass through a focused laser beam with a wavelength of 0.638

μm . Light from the focused laser beam was scattered by individual particles into the forward direction between the angles of 4° to 12° . Particles are sized using Mie scattering theory, assuming the particle shape is spherical, and for a specified refractive index. The approximate size range for the FSSP-100 in 15 size categories is 2.0 to 50 μm , and the approximate size range for the FSSP-300 in 31 size categories is 0.3 to 20 μm , but the size ranges are adjusted as a function of the refractive index, as described below and in Baumgardner and Clarke (1998). The sampling areas are 0.6 mm^2 and 0.05 mm^2 for the FSSP-100 and FSSP-300, respectively. The sampling volume of the instruments is the product of the sampling areas, aircraft air speed of the C-130, and sample rate. The sample rate of the data set used here is 1 Hz. Instrumentation response functions and number concentration derivations will be further discussed in the Appendix.

Since the FSSP-100 and FSSP-300 are optical counters, there are some problems that can occur when determining the size ranges of the bins. Pinnick *et al.* (1981) and Baumgardner and Clarke (1998) have pointed out that the theoretical Mie scattering curve is nonmonotonic through part of the FSSP-100 and FSSP-300 size range and suggested that some of the channels be combined. Calculations of the size distribution based on combining channels as suggested by Pinnick *et al.* (1981) and Baumgardner *et al.* (1989) result in a smoother distribution, as would be expected from any combination of channels, but have very little effect on the overall shape or derived concentrations (Kristament *et al.*, 1993). When the data were first evaluated, the FSSP-100 and -300 were not combined. Each probe was evaluated separately to determine if there was good agreement between regions of overlap. Figure 2.1 shows an example of the calculated size distribution for all 31 channels of the FSSP-300 and 15 channels of the FSSP-100

within the boundary layer. The overlap region between the two probes began at approximately 2 μm . From Figure 2.1, the size distribution for the FSSP-300 was much higher than the FSSP-100 by a factor of 10. The next step was to consider combining channels for each of the probes to create smoothed distributions with larger bins and perhaps reduce the disagreement; however, the threshold voltages were not available, and these must be used in redefining the FSSP channels using the corresponding pulse height voltages for each channel. The next option was combining data from the two probes in the overlap region, without double counting particles. The first channels in the FSSP-100 and FSSP-300 were considered to be questionable because of electronic noise and are often removed. In this work, data from the first channels of the FSSP-300 and FSSP-100 have been removed. In order to eliminate the problem of double counting particles, all other FSSP-100 channels were retained, but only channels 2 through 19 from the FSSP-300 were used, which span particle midpoints of ~ 0.45 to $3.5 \mu\text{m}$ (refer to Tables 2.2 and 2.3). The upper limit of channel 19 of the FSSP-300 was used to replace the lower limit of channel 2 of the FSSP-100, since they were close in value. Choosing the FSSP-100 for particle diameters $> 3.5 \mu\text{m}$ was more conservative since the FSSP-100 concentrations were lower than the FSSP-300. Thus our reported total number concentrations are probably conservative also. The combined size distributions span the approximate diameter range of $0.4 \leq D_p \leq 50 \mu\text{m}$. The particle diameters corresponding to the upper and lower bounds of each channel were determined by a spline-fit, smoothing algorithm applied through the theoretical Mie scattering efficiencies, with the instrument normalization constant specified from calibrations. As an example, Figure 2.2

displays the scattering cross section ($\text{cm}^2/\text{particle}$) for two refractive indices (1.33 and 1.58) and spline-fit, smoothing algorithms (Dr. Darrel Baumgardner, unpublished data).

Originally, the data sets were processed using a refractive index of 1.44. However, particle sizing is dependent on refractive index, which is determined by particle composition and relative humidity. Since particles were measured in their environment, the data sets were reprocessed for different refractive indices. The dry particle chemical composition was assumed constant and to be sea salt; variations in relative humidity altered the refractive index. Tables 2.2 and 2.3 show the mean diameters for channels of the FSSP-300 and FSSP-100, respectively, for all values of refractive index relevant for atmospheric particles in this study. These mean sizes differ from those specified by the manufacturer, which are based on calibration particles with a refractive index of 1.58. A total of 11 sets of channel diameters for indices of refraction ranging from 1.36 to 1.56 for non-absorbing particles were used.

Table 2.1 Measured and Derived Parameters (Baumgardner and Clarke, 1998).
The numbers in the brackets represent relative accuracies.

Measurement	Accuracy, %
Temperature (Rosemount)	± 1 [± 0.1]
Pressure (Rosemount)	± 0.05 [± 0.01]
Water Vapor (Lyman Alpha)	± 2 [± 0.05]
Relative Humidity (derived)	± 2 [± 0.05]
Number concentration (FSSP - 300)	± 15 [± 5]
Volume concentration (derived)	± 38 [± 10]
Effective radius (derived)	± 30 [± 10]
Scattering coefficient (derived)	± 30 [± 10]

Figure 2.1. Size distributions for the boundary layer (700 to 800 m) for the FSSP-300 (dashed lines) and the FSSP-100 (solid lines) for RP 11 (for particle size ranges 0.3 μm \leq 2.0 μm and 2.0 μm \leq 50 μm , respectively).

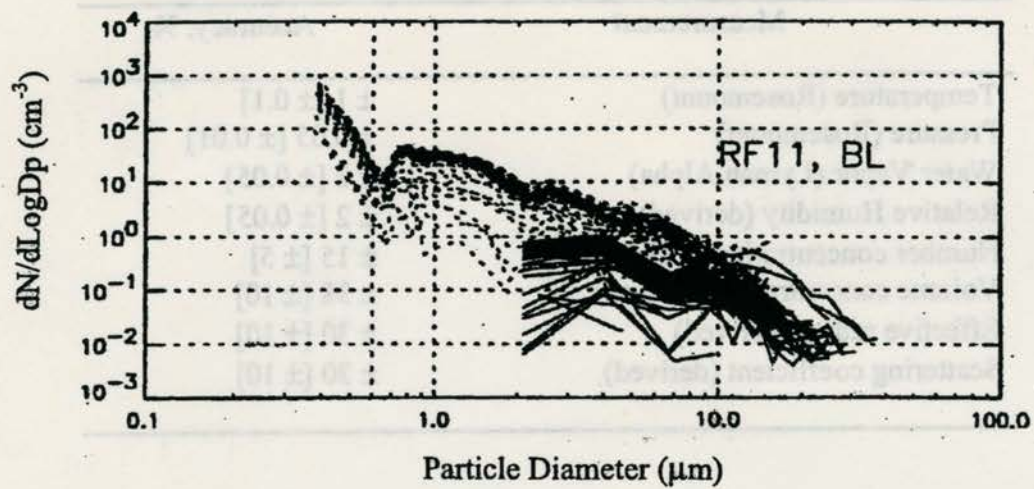


Figure 2.1 Size distributions for the boundary layer (300 to 900 m) for the FSSP-300 (dashed lines) and the FSSP-100 (solid lines) for RF 11 (for particle size ranges $0.3 \leq D_p \leq 20 \mu\text{m}$ and $2.0 \leq D_p \leq 50 \mu\text{m}$, respectively).

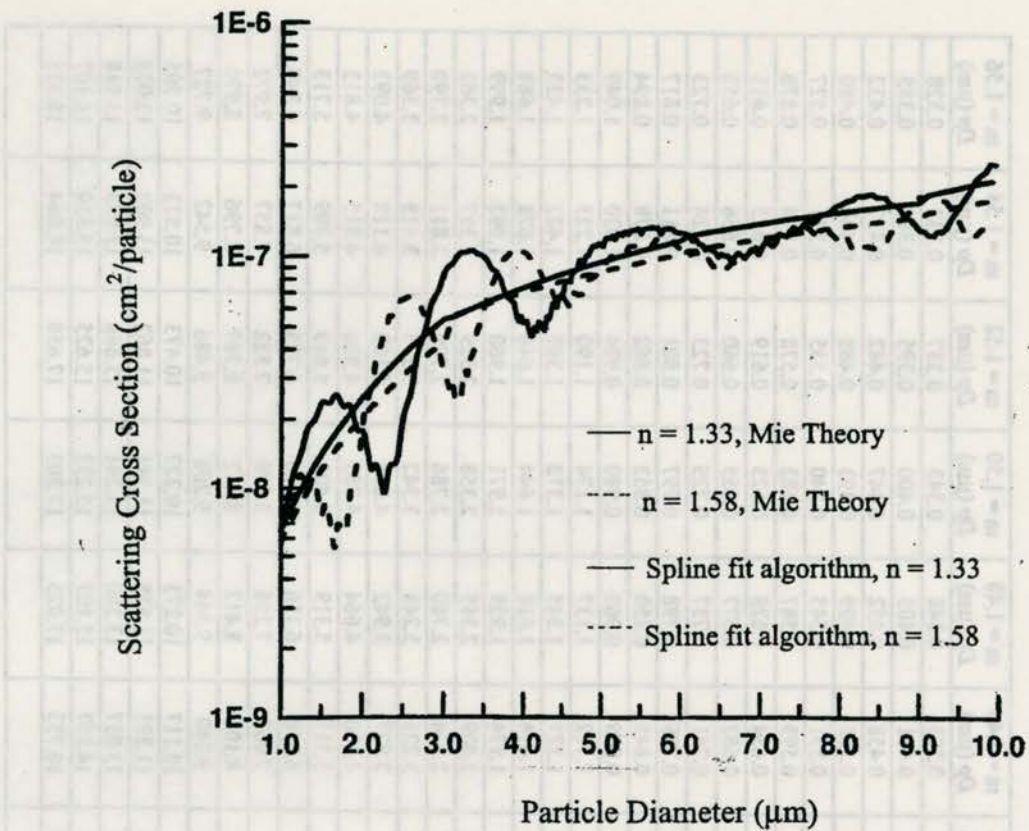


Figure 2.2 Scattering cross section ($\text{cm}^2/\text{particle}$) as a function of particle diameter ($1 \mu\text{m} < D_p < 10 \mu\text{m}$) for the $4^\circ - 12^\circ$ scattering angles for the FSSP-100 and real refractive indices of 1.33 (solid oscillating line) and 1.58 (dashed oscillating line). The spline-fit, smoothing algorithm is shown for 1.33 (solid line) and 1.58 (dashed line), provided by Dr. Darrel Baumgardner.

Table 2.2 FSSP-300 midpoints for each bin as a function of refractive index.

FSSP-300 Channels	m = 1.36 <i>D_p</i> (μm)	m = 1.38 <i>D_p</i> (μm)	m = 1.40 <i>D_p</i> (μm)	m = 1.42 <i>D_p</i> (μm)	m = 1.44 <i>D_p</i> (μm)	m = 1.46 <i>D_p</i> (μm)	m = 1.48 <i>D_p</i> (μm)	m = 1.50 <i>D_p</i> (μm)	m = 1.52 <i>D_p</i> (μm)	m = 1.54 <i>D_p</i> (μm)	m = 1.56 <i>D_p</i> (μm)
1	0.386	0.378	0.372	0.366	0.358	0.353	0.348	0.343	0.337	0.332	0.328
2	0.446	0.437	0.43	0.424	0.417	0.411	0.405	0.400	0.395	0.390	0.385
3	0.495	0.486	0.478	0.471	0.464	0.458	0.452	0.447	0.442	0.437	0.432
4	0.543	0.534	0.526	0.518	0.511	0.505	0.499	0.493	0.488	0.484	0.480
5	0.590	0.581	0.572	0.565	0.557	0.551	0.545	0.540	0.535	0.531	0.527
6	0.633	0.624	0.615	0.607	0.600	0.593	0.587	0.582	0.578	0.574	0.570
7	0.680	0.665	0.656	0.648	0.641	0.634	0.628	0.623	0.619	0.615	0.611
8	0.732	0.715	0.706	0.698	0.689	0.682	0.677	0.665	0.660	0.656	0.653
9	0.785	0.773	0.765	0.755	0.747	0.741	0.737	0.725	0.723	0.724	0.723
10	0.834	0.822	0.816	0.808	0.802	0.799	0.798	0.797	0.801	0.811	0.817
11	0.874	0.864	0.858	0.852	0.849	0.848	0.850	0.853	0.862	0.878	0.894
12	0.927	0.919	0.916	0.912	0.911	0.945	0.960	0.980	0.994	1.020	1.049
13	1.030	1.032	1.033	1.042	1.055	1.112	1.137	1.174	1.190	1.223	1.233
14	1.214	1.232	1.243	1.267	1.294	1.327	1.345	1.378	1.389	1.422	1.432
15	1.476	1.509	1.533	1.565	1.589	1.614	1.618	1.644	1.646	1.678	1.688
16	1.806	1.858	1.903	1.946	1.963	1.974	1.959	1.971	1.960	1.992	1.999
17	2.204	2.283	2.355	2.413	2.419	2.409	2.365	2.358	2.329	2.357	2.363
18	2.596	2.703	2.778	2.760	2.803	2.824	2.760	2.786	2.789	2.811	2.790
19	3.007	3.096	3.163	2.954	3.093	3.221	3.248	3.342	3.395	3.413	3.369
20	3.506	3.516	3.602	3.505	3.672	3.827	3.942	4.054	4.100	4.118	4.093
21	4.161	4.143	4.255	4.436	4.533	4.600	4.664	4.763	4.800	4.815	4.813
22	4.963	4.991	5.143	5.334	5.344	5.311	5.319	5.401	5.649	5.709	5.713
23	5.695	5.834	6.064	6.180	6.111	6.078	6.156	6.310	6.725	6.817	6.849
24	6.376	6.634	6.949	6.988	6.933	7.067	7.256	7.479	7.822	7.857	7.972
25	7.237	7.468	7.839	7.910	7.963	8.105	8.412	8.412	8.769	8.796	8.970
26	8.334	8.426	8.733	8.767	8.917	9.040	9.344	9.208	9.486	9.542	9.727
27	9.331	9.478	9.687	9.671	9.881	10.117	10.273	10.227	10.473	10.523	10.705
28	10.335	10.632	10.883	10.890	11.166	11.391	11.575	11.541	11.862	11.902	12.078
29	11.815	12.100	12.424	12.466	12.832	13.037	13.260	13.241	13.668	13.693	13.918
30	13.460	13.724	14.133	14.568	14.624	14.867	15.107	15.232	15.625	15.829	16.107
31	15.051	15.418	15.799	16.293	16.420	16.753	17.023	17.303	17.658	18.064	18.355

Table 2.3 FSSP-100 midpoints for each bin as a function of refractive index.

FSSP-100 Channels	m = 1.36 D_p (μm)	m = 1.38 D_p (μm)	m = 1.40 D_p (μm)	m = 1.42 D_p (μm)	m = 1.44 D_p (μm)	m = 1.46 D_p (μm)	m = 1.48 D_p (μm)	m = 1.50 D_p (μm)	m = 1.52 D_p (μm)	m = 1.54 D_p (μm)	m = 1.54 D_p (μm)
1	2.089	2.100	2.370	2.443	2.199	2.294	2.294	2.311	2.216	2.234	2.181
2	4.017	3.984	4.618	4.791	4.252	4.357	4.307	4.316	4.086	4.067	3.934
3	6.690	6.618	7.007	7.393	7.301	7.337	7.190	7.062	6.490	6.802	6.656
4	9.292	9.333	9.676	10.063	10.129	10.376	10.326	10.122	9.444	9.913	9.806
5	11.291	11.454	12.089	12.232	12.383	12.610	12.565	12.435	12.087	12.039	11.971
6	13.366	13.484	14.238	14.410	14.707	14.978	14.901	14.848	14.342	14.442	14.332
7	15.704	15.882	16.739	17.014	17.375	17.767	17.665	17.668	17.016	17.290	17.169
8	18.505	18.731	19.691	20.338	20.515	20.998	20.978	21.082	20.364	20.619	20.369
9	21.647	21.845	22.912	23.913	23.966	24.530	24.594	24.798	23.979	24.291	23.876
10	24.810	25.093	26.320	27.492	27.596	28.371	28.241	28.662	27.688	27.969	27.651
11	27.871	28.381	29.665	31.017	31.194	32.141	31.700	32.412	31.259	31.506	31.471
12	30.868	31.536	32.906	34.344	34.655	35.677	35.080	35.918	34.654	35.017	35.152
13	33.815	34.455	36.090	37.483	37.974	38.956	38.534	39.017	38.299	38.496	38.588
14	36.658	37.342	39.325	40.422	41.162	42.079	41.972	41.998	41.947	41.912	41.947
15	39.523	40.374	42.479	43.381	44.330	45.336	45.299	45.310	45.289	45.278	45.289

CHAPTER 3. DATA SET

Section 3.1. Removal of in-cloud data

Only aerosols in non-cloudy regions were included in the analysis. Therefore, an in-cloud criterion was applied to remove those points from the data set. A relevant indicator of the presence of clouds is the number concentration of particles of larger sizes, as measured by the FSSP-100 (Kristament *et al.*, 1993). Baumgardner and Clarke (1998) used $N_{100} > 5 \text{ cm}^{-3}$ to define cloud, where N_{100} is the total number concentration measured by the FSSP-100. Hudson *et al.* (1998) used a criterion of $N_{100} > 1 \text{ cm}^{-3}$. In this work, three criteria ($N_{100} > 1 \text{ cm}^{-3}$, $N_{100} > 5 \text{ cm}^{-3}$, and $N_{100} > 10 \text{ cm}^{-3}$) were tested. In-cloud times generated with each criterion were compared with the visual record from research flight video tapes provided by the RAF. The comparisons were most consistent for $N_{100} > 1 \text{ cm}^{-3}$, and therefore this criterion was used for cloud removal from the aerosol data set. After the removal of cloudy regions, data corresponding to relative humidities greater than 100% were also removed; only a few such points were found.

Section 3.2. Number concentration processing

Number concentrations were defined in terms of two particle size groupings, $0.5 \leq D_p \leq 50$ microns, N_1 and $2.0 \leq D_p \leq 50 \mu\text{m}$, N_2 . As briefly described in Chapter 2, the first channel of each probe were removed and only part of the FSSP-300 channels were used because of instrument overlap with the FSSP-100. For comparison with Kristament

et al. (1993), a particle diameter of 0.5 μm was considered as the lower limit for N_2 , which usually was channel 4 or channel 5 of the FSSP-300, depending on refractive index. For the lower limit of N_2 , 2.0 μm was selected, corresponding to, channels 17 – 19 of the FSSP-300. Concentration data were then corrected to standard temperature and pressure. The remaining aerosol data were averaged for every 100 seconds and binned into 100-meter altitude increments. If after cloud removal, fewer than 20 records remained to be averaged in any 100-sec time period, that time period was removed from the data set. Figure 3.2.1 shows a time line of unaveraged N_{100} and averaged N_2 concentrations for each research flight for times periods of 0:00 – 7:30 UTC. The plus signs represent N_{100} concentrations, and the open circles represent N_2 concentrations for $2.0 \leq D_p \leq 50 \mu\text{m}$ for combined probes. The dashed line represents a separation between concentrations greater than and less than 1.0 cm^{-3} . Some N_2 concentrations appear to be slightly higher than the 1.0 cm^{-3} line; however, this is an effect of pressure and temperature corrections and averaging.

Section 3.3. Estimated lower detection limit

The low volumetric sample sizes and low particle number counts, particularly above the boundary layer, can lead to low estimated aerosol number concentrations. Even for 100-second averaging, the statistical significance of the computed concentrations may be questionable. To address this, we estimated the lower detection limit (*LDL*) of the FSSP probes using the following procedure. A 20 sec segment of low-concentration data was selected as an experimental “blank”, and the mean (\bar{X}_b) and standard deviation

(s_b) of the number concentration computed (Skoog *et al.*, 1996). The minimum detection limit was then estimated from

$$LDL = \bar{X}_b + ts_b \sqrt{\frac{N + N_b}{NN_b}} \quad (3.3.1)$$

where N is the number of data points averaged (usually 100), N_b = the number of observations in the blank (20), and t was obtained for the 95% confidence level and for $n = N + N_b - 2$ degrees of freedom. Three different low concentration segments were selected to verify consistency in the estimates. The LDL was estimated to be 0.040 cm^{-3} , for total number concentrations of particles having sizes $0.5 \leq D_p \leq 50$ microns (N_1), as well as for those with $2.0 \leq D_p \leq 50$ microns (N_2). Detection limits were also calculated for surface area and volume distributions using the same procedure. For S_1 and S_2 , the LDL was 0.146 and $1.015 \mu\text{m}^2 \text{ cm}^{-3}$. For V_1 and V_2 , the LDL was 0.036 and $0.4934 \mu\text{m}^3 \text{ cm}^{-3}$. The LDL s for the ambient scattering coefficients were 9×10^{-5} and 0.0006 km^{-1} for N_1 and N_2 , respectively. Any computed concentrations lower than the LDL estimated by equation 3.3.1 cannot be distinguished from the zero at the 95% confidence level. Therefore, the average of the appropriate LDL and zero was then used to replace any 100-sec average that fell below the LDL .

Section 3.4. Determination of aerosol refractive index and water content

Since the data are from a marine environment, we assumed that the chemical composition of the large particles would be dominated by sea salt (Fitzgerald, 1991; Gras and Ayers, 1983; Quinn *et al.*, 1998). The water content and density of the aerosol were estimated from the correlations provided by Tang *et al.* (1997). Figure 3.4.1 displays the

particle mass change with respect to the dry sea salt mass, w/w_o , plotted as a function of RH for sea salt and NaCl. The dashed curves represent the hydrated behavior of a pure NaCl particle, and the solid lines represent that for a sea salt particle. Sea salt particles gradually take up water until about 70% RH. At approximately 74% RH, a dry sea salt particle deliquesces or rapidly picks up more water to become a homogeneous solution droplet. However, once deliquesced, with decreasing RH, the droplet loses water by evaporation but remains a metastable solution until efflorescence occurs at about 46 to 48% RH (Tang *et al.*, 1997). For RH > 46% the water content was assumed to follow the efflorescence curve. For RH ≤ 46%, it was assumed that the particles existed in crystalline form with a density of 2.165 g cm⁻³, a refractive index of 1.544, and a solute weight percent of 100.

To determine the water content, it was assumed that the particle was in equilibrium with its environment, such that RH = a_w , where a_w is the solution water activity. Relative humidities from the 100-second averages were used. Polynomials of the form

$$a_w = 1.0 + \sum C_i x^i \quad (3.4.1)$$

where a_w is a best fit curve as a function of x (solute weight percent), and C_i is the polynomial coefficient, are provided by Tang *et al.* (1997). Values of solute weight percent, x , versus a_w were then fit by

$$x = -1717.1a_w^5 + 5621.4a_w^4 - 7412.0a_w^3 + 4908.0a_w^2 - 1689.0a_w + 288.21 \quad (3.4.2)$$

Using the value of x determined from the average RH, the density was calculated using polynomial coefficients from Table 3.4.1 from Tang *et al.* (1997) in the equation

$$d = 0.9971 + \sum A_i x^i \quad (3.4.3)$$

where x is the weight percent of total solutes and A_i is the polynomial coefficient for density. The constants used in equations (3.4.1) and (3.4.3) are shown in Table 3.4.1.

After the densities and the solute weight percents were calculated, they were averaged for every 100-seconds and binned in 100-meter altitude increments.

By definition, the molal refraction, R , of either a pure substance or a homogeneous mixture of molal volume V and refractive index, n , is given by (Moelwyn-Hughes, 1961; Tang *et al.*, 1997)

$$R = \frac{V(n^2 - 1)}{(n^2 + 2)} \quad (3.4.4)$$

The molal volume in equation 3.4.4 is given by

$$V = \frac{1}{d}(y_1 M_1 + y_2 M_2) \quad (3.4.5)$$

where y_1 and y_2 are mole fractions of the solvent water and total solute ions, M_1 is the molecular weight of the solvent, and M_2 is the average ionic weight of the solute ions.

Using the solution composition as a function of RH to compute R and V , equation 3.4.4 can then be rearranged for n :

$$n = \sqrt{\frac{2R + V}{V - R}} \quad (3.4.6)$$

The corresponding calibration for each probe for the computed n , interpolated from available calibrations, was then used to process data.

The wet (M_w) and dry (M_d) sea salt mass concentrations can be computed from x , ρ , and volume concentrations. First, the ambient, or wet, sea salt mass concentration is given by

$$M_w = \frac{\pi}{6} \rho \int_0^{\infty} Dp^3 \frac{dN}{dDp} dDp \approx \frac{\pi}{6} \rho \sum_{i=1}^k Dp_i^3 N_i \quad (3.4.7)$$

where ρ is the density, Dp_i is the mean diameter of bin i , N_i is the number concentration in bin i , and k is the total number of bins. The dry sea salt concentrations can be obtained from the wet using

$$M_d = \frac{x}{100} M_w \quad (3.4.8)$$

In Table 2.2 and 2.3, the effect of changes in aerosol refractive index on particle optical size is shown. Although the particle sizes shift only slightly with refractive index, the particle size change influences the surface area concentrations by Dp^2 and the volume concentrations by Dp^3 , and this effect is thus magnified. Kristament *et al.* (1993) used the manufacturer's calibration in their work, and ignored the effects of particle composition on the optical size. Baumgardner and Clarke (1998) estimated the maximum estimated error in derived size to be approximately 20%, if the particle refractive index is known. When the refractive index is not known the uncertainty increases, and the magnitude of the resultant error is dependent upon particle size (Baumgardner and Clarke, 1998). The error in the number concentrations is estimated as approximately 15%, which is largely due to uncertainties in the sample volume (Baumgardner *et al.*, 1992). For aerosol volume concentrations, Baumgardner and Clarke (1998) estimate that their assumption of an average particle refractive index of 1.40, regardless of RH or composition variations in the sample, could lead to errors greater than 50%. We expect the assumptions applied in this work to lead to uncertainties of similar magnitudes.

Section 3.5. Optical properties

Since sea salt absorbs negligibly in the visible (550 nm), aerosol extinction is approximately equal to aerosol scattering. The scattering coefficient is a function of the size distribution and the refractive index and is computed by the following equation:

$$b_{sp} = \int_0^{\infty} Q_{scat}(Dp_i, \lambda, n) \frac{\pi}{4} Dp^2 \left(\frac{dN}{d \log Dp} \right) d \log Dp \approx \frac{\pi}{4} \sum_{i=1}^k Q_{scat}(Dp_i, \lambda, n) Dp_i^2 N_i \quad (3.5.1)$$

The term Q_{scat} in the integral is the well-known Mie scattering efficiency, which (assuming homogeneous spheres) is a function of particle size (Dp), the wavelength of the scattered light (λ), and the index of refraction of the particles (n). For this study we chose one wavelength near the midpoint Dp of the visible (550 nm) as in Hegg *et al.* (1996) and Quinn *et al.* (1998). The b_{sp} values were averaged for every 100 seconds in 100 meter altitude increments. The optical depth was then computed from

$$\tau = \int_0^{\infty} \overline{b_{sp}}(z) dz \approx \sum_{j=1}^l \overline{b_{sp}}_j z_j \quad (3.5.2)$$

where l represents each 100 m layer, $z_j = 100$ m, and $\overline{b_{sp}}_j$ is the layer-averaged scattering coefficient.

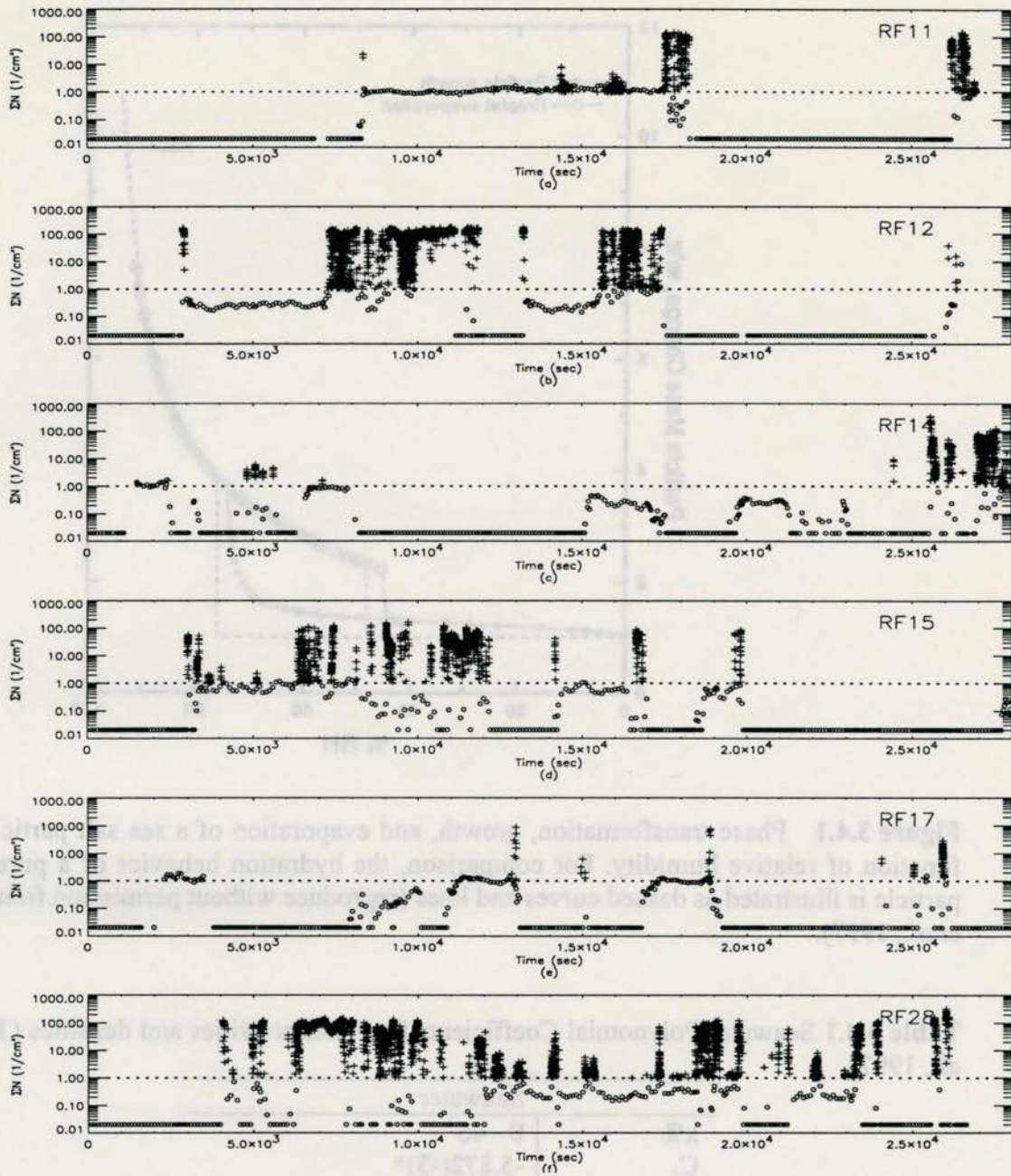


Figure 3.2.1 A time line of cloud droplet, N_{100} and N_2 concentrations for a) RF 11, b) RF 12, c) RF 14, d) RF 15, e) RF 17, and f) RF 28. The plus signs represent the N_{100} concentrations, and the open circles represent N_2 concentrations.

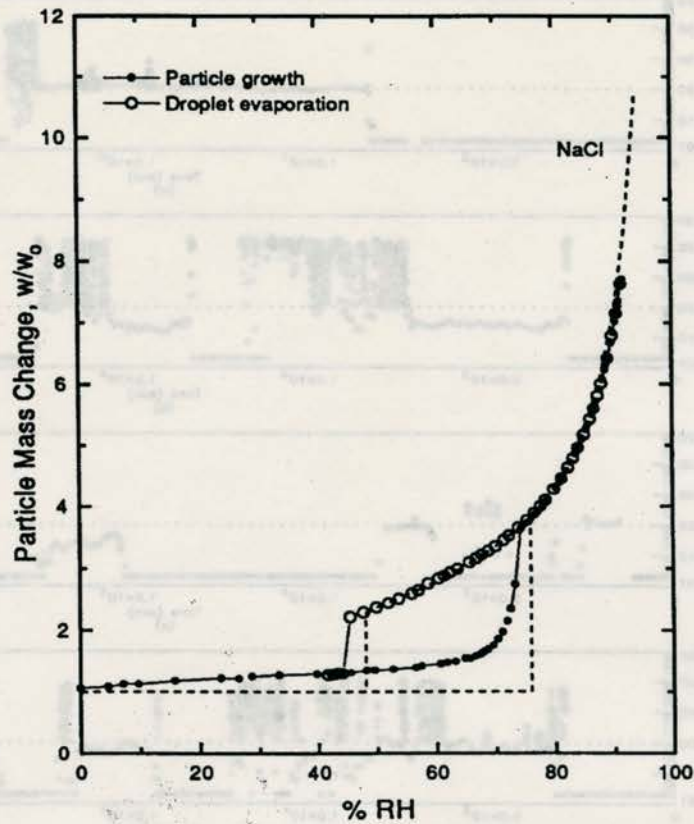


Figure 3.4.1 Phase transformation, growth, and evaporation of a sea salt particle as a function of relative humidity. For comparison, the hydration behavior of a pure NaCl particle is illustrated as dashed curves and lines (reproduce without permission from Tang *et al.*, 1997).

Table 3.4.1 Seawater Polynomial Coefficients for water activities and densities (Tang *et al.*, 1997).

Seawater	
x%	0 - 46
C ₁	-5.872(-3)*
C ₂	1.24(-4)
C ₃	-1.688(-5)
C ₄	3.105(-7)
C ₅	-1.44(-9)
A ₁	7.93(-3)
A ₂	-4.28(-5)
A ₃	2.52(-6)
A ₄	-2.35(-8)

* Read -5.872(-3) as -5.872×10^{-3}

CHAPTER 4. FSSP RESULTS

Section 4.1. Vertical profiles of number concentrations

Vertical profiles of cloud droplet number concentrations, obtained from the in-cloud points that have been removed from the aerosol data set, are shown for each flight in Figures 4.1.1a through 4.1.1f. The cloud droplet number concentrations in Figure 4.1.1 have been summed from the channel corresponding to $\sim 2 \mu\text{m}$ to the upper limit of the FSSP-100 ($\sim 50 \mu\text{m}$). Figures 4.1.2a through 4.1.2f show vertical profiles of aerosol number concentrations N_i ($0.5 \leq D_p \leq 50 \mu\text{m}$) for the non-cloudy regions. Concentrations at or below the *LDL* that have been replaced by the average of the *LDL* and zero, which are easily distinguished in Fig. 4.1.2, with many points above the *LDL* remaining at higher altitudes. A comparison of Figures 4.1.1 and 4.1.2 suggests that some elevated large particle concentrations were associated with clouds, particularly above the boundary layer (altitude, z , $> 900 \text{ m}$). The boundary layer was defined to be consistent with that chosen by Kristament *et al.* (1993), as explained in section 4.2. Although in-cloud data have been removed using the criteria discussed in section 3.1, there are still areas of relatively high RH in the free troposphere, which could be cloud boundaries or residuals of old clouds that have dissipated. These regions are sometimes associated with high large particle number concentrations. These relationships will be explored further in Chapter 5.

For comparison with the present data set, the coarse mode number concentration fit ($0.5 \leq D_p \leq 10 \mu\text{m}$) determined by Kristament *et al.* (1993) for $z \leq 2400$ m is shown in Figure 4.1.2 by the solid line:

$$\log\left[\sum N_1\right] = (0.3 - 0.52h) \quad (4.1.1)$$

where h is the height in km. The standard deviation determined for the original fit (2.3 in N_1) is shown by the dotted line. Kristament *et al.* (1993) justified the choice of the log-linear fit on the basis that data for total aerosol counts were strongly skewed toward low counts when examined on a linear scale. Using a linear regression on the log of particle concentrations is reasonable because the dependence on individual covariates is exponential. Further, they point out that the functional form has analogues in air pressure and density, which have exponential dependencies on altitude. We choose to use the same functional form for fits in this work. The data from ACE-1 show some similar behavior with altitude, although many of the points lie outside the one standard deviation line. In particular, particle number concentrations in the boundary layer are generally higher than those suggested by one standard deviation from the fit equation, except for RF 28. Table 1.1.1 also indicates that RF 28 had the lowest mean number concentrations among all flights for altitudes < 2400 m. Low-level clouds were frequently encountered in RF 28, as seen in Fig. 4.1.1f, and drizzle within the boundary layer was reported in the flight log; it is likely that the lower number concentrations encountered in this mission were influenced by wet removal processes.

The data for $0.5 \leq D_p \leq 50 \mu\text{m}$ and $z < 2400$ m from all flights considered here were least squares fit to an equation of the same form as used by Kristament *et al.* (1993):

$$\log[\Sigma N_1] = (1.0056 - 0.769h) \quad (4.1.2)$$

which yielded a standard deviation of 3.72 in N_1 , and a correlation coefficient $r^2 = 0.479$, very similar to that obtained by Kristament *et al.* (1993). Figure 4.1.3 shows $\log[\Sigma N_1]$ as a function of altitude. Equation 4.1.2 was superimposed to show the large variation in $\log[\Sigma N_1]$. As can be seen from the slope and intercept of equation (4.1.2), and surmised from Fig. 4.1.2, N_1 was generally higher than that determined for the New Zealand / SW Pacific region by Kristament *et al.* (1993), and dropped off somewhat more rapidly with altitude.

Vertical profiles of the total particle number concentration in the size fraction $2 \leq Dp \leq 50 \mu\text{m}$ (N_2) are shown in Figure 4.1.4, with equation 4.1.1 superimposed. The number concentrations are significantly reduced from those shown in Fig. 4.1.2, suggesting that most of the contribution to N_1 is in the $0.5 \leq Dp \leq 2 \mu\text{m}$ size range. The fit to the data for $2 \leq Dp \leq 50 \mu\text{m}$ and $z < 2400 \text{ m}$ from all flights considered here was

$$\log[\Sigma N_2] = (-0.2445 - 0.6339h) \quad (4.1.3)$$

with a standard deviation of 3.18 in N_2 , and a correlation coefficient $r^2 = 0.45$. Figure 4.1.5 shows $\log[\Sigma N_2]$ as a function of altitude. Equation 4.1.3 was superimposed for comparison. The average altitude variation of N_2 is similar to that found for N_1 , although the profiles for individual flights can be quite different. For example, the effects of drizzle on the vertical profiles in RF 28 were already noted for Fig. 4.1.2 and are also apparent in Figure 4.1.4.

Very few particles larger than $2 \mu\text{m}$ were observed above 2400 m. Only in RF 14, RF 17 and RF 28 were there occasional significant N_2 concentrations at higher altitudes.

These flights explored, respectively, cumulus outflow regions (~4100 m, ~5200 m, and 5500 m); deep widespread cumuli; and stratocumuli, above a drizzling boundary layer (Table 1.1.1). The presence of regions of deep convection thus appears to be linked with the lofting of particles larger than 2 μm to the free troposphere. For example, cloud tops were reported at ~6100 m in RF 17, and cloud outflow regions at ~2700 m; significant concentrations of both N_1 and N_2 particles were observed at these altitudes. Research flights containing cloud dissipation, deep convection, cloud outflow, and areas of high relative humidity above 2400 m denoted enhanced N_1 and N_2 concentrations.

Wind speeds at the surface may also play a role in the number concentrations of large particles above the BL, since they should influence the strength of the source of sea salt particles. Figure 4.1.6 shows vertical profiles of wind speed for each of the flights. Relatively low surface wind speeds ($< 10 \text{ m s}^{-1}$) were observed during RF 12, and 15; both low and high ($> 10 \text{ m s}^{-1}$) surface winds were encountered in RF 14. Figure 4.1.7 a) and b) show a correlation of $\sum N_1$ and $\sum N_2$ as a function of wind speed for $z < 300 \text{ m}$.

The fits to the data for $\sum N_1$ and $\sum N_2$ as a function of wind speed for $z < 300 \text{ m}$ from all flights considered here were

$$\sum N_1 = 0.1386ws + 9.4191 \quad (4.1.4)$$

$$\sum N_2 = 0.0191ws + 0.4585 \quad (4.1.5)$$

where ws is the wind speed in m s^{-1} . The standard deviation for $\sum N_1$ was 1.44 with a correlation coefficient of 0.0026. The standard deviation for $\sum N_2$ was 0.08 with a correlation coefficient of 0.0182. Although Fig. 4.1.7 a) and b) do show a very low correlation between number concentrations as a function of wind speed, a slight positive

slope can be seen for both dependent variables. For stronger winds ($w_s > 10 \text{ m s}^{-1}$) number concentrations were high near the surface, which can be seen for RF 11, 14, 17, and 28 for Figures 4.1.2 and 4.1.4. Few N_2 particles were encountered above the BL in the two flights with low wind speed, whereas relatively high concentrations were seen in most of those flights with high surface winds. The exception is RF 11, but convective activity was not noted for this RF, so while N_2 concentrations near the surface are substantial they are not observed above the BL. In the other cases, high wind speeds at the surface were likely coupled with the same meteorological conditions that created convection. That is, a synoptic scale disturbance was most likely destabilizing the atmosphere, leading to convective activity, as well as increased surface winds.

Tables 4.1.1, 4.1.2, and 4.1.3 show the averaged total number (N_1 and N_2), surface area (S_1 and S_2), and volume (V_1 and V_2) concentrations for $0.5 \leq D_p \leq 50 \text{ }\mu\text{m}$ and $2.0 \leq D_p \leq 50 \text{ }\mu\text{m}$, respectively, for various altitude levels. The N_1 , S_1 , and V_1 ranged from $0.07 - 16.40 \text{ cm}^{-3}$, $0.13 - 94.62 \text{ }\mu\text{m}^2 \text{ cm}^{-3}$, and $0.02 - 304.45 \text{ }\mu\text{m}^3 \text{ cm}^{-3}$, respectively. The N_2 , S_2 , and V_2 ranged from $0.02 - 10.01 \text{ cm}^{-3}$, $0.51 - 84.27 \text{ }\mu\text{m}^2 \text{ cm}^{-3}$, and $0.25 - 302.40 \text{ }\mu\text{m}^3 \text{ cm}^{-3}$. Below 2400 m, the average concentrations of both N_1 and N_2 particles were generally above the *LDL*. However, at higher altitudes, N_2 concentrations in most of the RFs were at or below the *LDL*, as seen from computed mean concentrations equal to the *LDL/2* (0.02 cm^{-3}). Exceptions are RF 14, 17, and 28, which also had significant concentrations of S_1 and V_2 at these altitudes, for the reasons discussed above in association with vertical profiles of number concentrations. In RF 12, the surface area and volume concentrations in both size classes were quite high in the 900 – 2400 m layer, which coincided with cloud levels. The contributions of N_2 particles to the surface area

and volume concentrations above 2400 m are substantial in all flights, suggesting that supermicron particles should be included in estimates of aerosol optical depth.

Section 4.2. Number size distributions from the FSSP-300 and FSSP-100

In accordance with the proposed altitude classifications from Kristament *et al.* (1993), the number size distributions were grouped into 3 layers: $z \leq 900$ m, the “boundary layer” (BL); $2400 \leq z \leq 3000$ m, the “mid troposphere” (MT); and $z \geq 4250$ m, the “free troposphere” (FT). Although Kristament *et al.* (1993) do not discuss in detail their choice of layer definition, it was found for our cases that 900 m was always well within the boundary layer. Figure 4.2.1 shows temperature as a function of altitude. The inversion layer is denoted by the dashed line, which usually represents a sharp decrease in particle concentrations and defines the location of the BL top. The BL top ranged from 900 to 1500 m, which is shown in Figure 4.2.1. The choice of $2400 \leq z \leq 3000$ m for the MT was also seen to be well above the BL for ACE-1. The level of convective outflow was usually above 4000 m, distinguishing FT from MT. Thus, for consistency with Kristament *et al.* (1993) results, we chose to use the same altitude classification scheme. The size distributions in the BL were markedly different between flights (Figures 4.2.2a to 4.2.2f). As expected, the maximum peaks are near the lower size limit ($\sim 0.4 \mu\text{m}$). The three vertical grid lines appearing on each graph are a visual aid and are placed at 0.6, 1.0, and $10 \mu\text{m}$. A minimum in the distribution generally occurs near $0.6 - 0.7 \mu\text{m}$. A secondary peak occurs near $10 \mu\text{m}$ and contributes significantly to the volume distributions although not to the number concentrations. Within the BL particles as large as $20 - 30 \mu\text{m}$ are frequently found.

The BL size distribution for RF 28 differs markedly from the other flights, particularly for particles with $D_p < 1 \mu\text{m}$, for which the number concentrations are greatly suppressed, probably due to the drizzle observed within the BL. Interestingly, the abundance of particles in the mode near $10 \mu\text{m}$ is not substantially different than that observed in other RFs. This is probably because local sources (sea spray) are active and replenishing this population, whereas drizzle removal acts as a permanent sink for the longer-lived smaller particles that has both local and long-range sources.

The size distributions for the MT are shown in Figure 4.2.3. Unlike the data from the other RFs, the size distributions for RF 17 and 28 extend beyond $D_p = 2 \mu\text{m}$, and have secondary peaks near $\sim 10 - 15 \mu\text{m}$. From Figure 4.4.1, clouds were found in the mid-troposphere for these flights, and the moisture associated with these fields could enhance large particle concentrations. Some cloudy regions were also sampled in the MT level in RF 14. The size distributions in that case have higher concentrations near $1 \mu\text{m}$ than do RF 11, 12 and 15, but no significant contributions from particles with $D_p > 2 \mu\text{m}$.

Figure 4.2.4 shows the FT size distributions. Two modes of larger particles (at $D_p \sim 2 \mu\text{m}$ and $D_p \sim 10 \mu\text{m}$) are seen in the data for RF 14, 17 and 28. These flights have already been identified as having the highest N_2 levels above the BL, were associated with convection in the sampling region, and except for RF 28, had cloudy regions in the FT layer. Although clouds were not directly encountered in RF 28, samples with $D_p > 2 \mu\text{m}$ did correspond to regions of relatively high relative humidities ($\text{RH} > 70\%$), suggesting they were associated with the transport of moisture, probably through cloud venting.

Section 4.3. Sea salt mass concentrations

Dry sea salt mass concentrations near the surface ($\sim 30 \leq z \leq 100$ m) were calculated as described in section 3.4, and are plotted as functions of wind speed in Figure 4.3.1. Data from ambient particles in the size range $0.5 \leq D_p \leq 50 \mu\text{m}$ were included, since this size range is most directly applicable to previously reported fits from impactor data. Derived mass concentrations range from 2 to $30 \mu\text{g m}^{-3}$ and increase strongly with increasing wind speeds. Also shown in Fig. 4.3.1 are the fits to the data of Lovett (1978) and Gras and Ayers (1983) suggested by Fitzgerald (1991). The sea salt mass concentrations and their variation with wind speed are generally closest to the observations of Gras and Ayers (1983). Table 4.3.1 shows the average derived sea salt mass concentrations for $z \leq 100$ m for each flight. The uncertainty in estimating the mass is greatly affected by uncertainties in volume concentrations, which could lead to errors greater than 50%. The assumptions about aerosol density that were applied also increase the uncertainty of these estimates. The effects of other applied assumptions on calculated mass concentrations will be further explored in Chapter 5.

Section 4.4. Scattering properties

Combining data sets from various platforms, Murphy *et al.* (1998) showed that sea salt particles dominated the total aerosol scattering and backscattering coefficients during ACE-1. Assuming the large particles examined here are primarily sea salt and water and using the methodology described in section 3.5, we calculated the mean, ambient scattering coefficients ($\overline{b_{sp}}$) as functions of altitude for both N_1 and N_2 particles, shown in Figures 4.4.1a and 4.4.1b, respectively. For RF 11, 12, and 15, $\overline{b_{sp}}$ decreases

with altitude below 2 km and remains low at higher altitudes. However, high values of $\overline{b_{sp}}$ were found aloft ($z > 2400$ m) for RF 14, 17, and 28, corresponding to the contributions from N_2 particles to the upper-level size distributions in these flights. In the BL ($z \leq 900$ m), $\overline{b_{sp}}$ values range from ~ 0.002 to 0.08 km^{-1} for N_1 particles, and ~ 0.001 to 0.05 km^{-1} for N_2 . In the MT and FT ($z > 2400$ m) $\overline{b_{sp}}$ ranges from ~ 0.00005 to 0.05 km^{-1} for N_1 , and 0.0003 to 0.04 km^{-1} for N_2 . Thus the larger N_2 particles can play a non-negligible role in the scattering budget, both in the BL and aloft.

Table 4.4.1 displays location, instrumentation, wavelength, and total light scattering coefficients reported in the literature for various research experiments. Our total light scattering coefficients near the surface (shown in Figure 4.4.1) are reasonably consistent with those studies. Baumgardner and Clarke (1998) reported lower total scattering values for some of the same flights studied here. Total scattering coefficients are greatly affected by the refractive index. Baumgardner and Clarke (1998) chose to use a refractive index of 1.40. Assuming a constant value for the refractive index neglects the variations in particle size and composition that can alter the total scattering coefficients. The total light scattering values reported by Quinn *et al.* (1998) show for particles in the supermicron range ($1.0 \leq D_p \leq 10 \text{ }\mu\text{m}$) are much higher than those for particles in submicron range ($D_p < 1.0 \text{ }\mu\text{m}$). Values observed by Remer *et al.* (1997) at higher altitudes are larger than generally observed in the ACE-1 data set, but the Atlantic is also substantially more influenced by anthropogenic emissions than is the ACE-1 region.

Utilizing the measured altitude dependence of $\overline{b_{sp}}$ as illustrated in Figure 4.4.1, aerosol optical depths (τ) have been calculated and are shown in Table 4.4.2. For N_1 and N_2 particles, $0.043 \leq \tau \leq 0.083$ and $0.017 \leq \tau \leq 0.038$, respectively. From a global

analysis of satellite data, Durkee *et al.* (1991) estimated optical depths in the visible ($\lambda = 690$ nm) over the ACE-1 study region of ~ 0.05 to 0.15 . Toon and Pollack (1976) reported optical depths of 0.05 to 0.14 at 500 nm wavelength, for measurements of marine aerosol made at all latitudes. The optical depths over the Northern Hemisphere from the vertical integration of b_{sp} reported by Remer *et al.* (1997) was 0.30 for $z \leq 3000$ m. The values derived here for the contribution from large particles only ($D_p \geq 0.5$ μm) are well within these estimates. Quinn *et al.* (1998) reported that 30 ± 4 % of total light scattering in the marine boundary layer was due to submicron sea salt particles and that 68 ± 4 % was due to supermicron sea salt particles. Since most of the contribution to optical depth occurs in the boundary layer, it is likely that particle sizes not considered in this work ($D_p < 0.5$ μm) would only make up a small portion of the optical depth. The ACE-1 project provided a comprehensive study of aerosol optical properties. Observations from satellite platforms, in order to study aerosol and cloud optical properties, were provided aboard the *Discoverer* ship and the C-130 aircraft (P. Durkee *et al.*, manuscript in preparation, 1998).

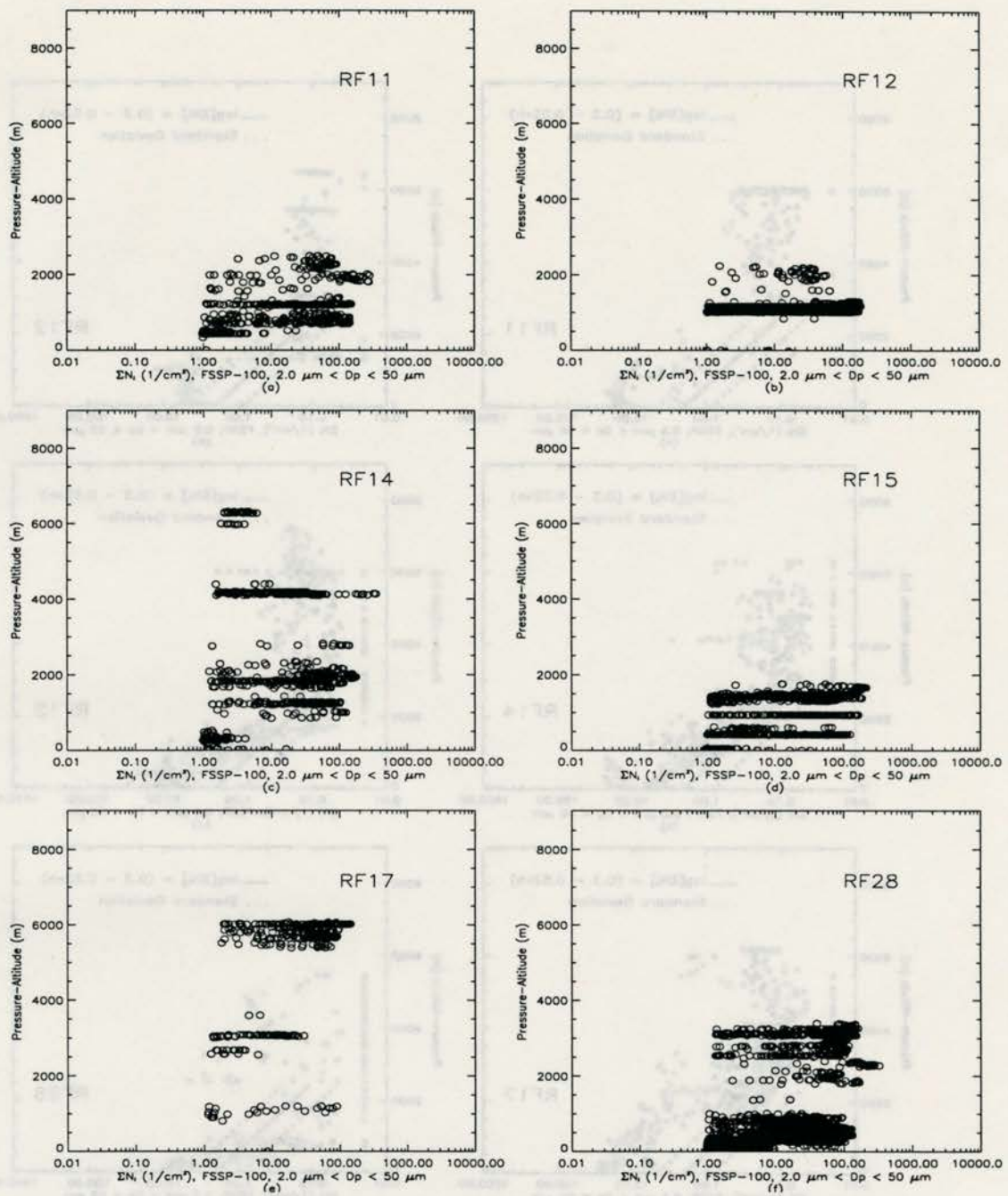


Figure 4.1.1 N_{100} concentrations as a function of altitude for the FSSP-100 (for particle sizes $2.0 \leq D_p \leq 50 \mu\text{m}$): a) RF 11, b) RF 12, c) RF 14, d) RF 15, e) RF 17, and f) RF 28.

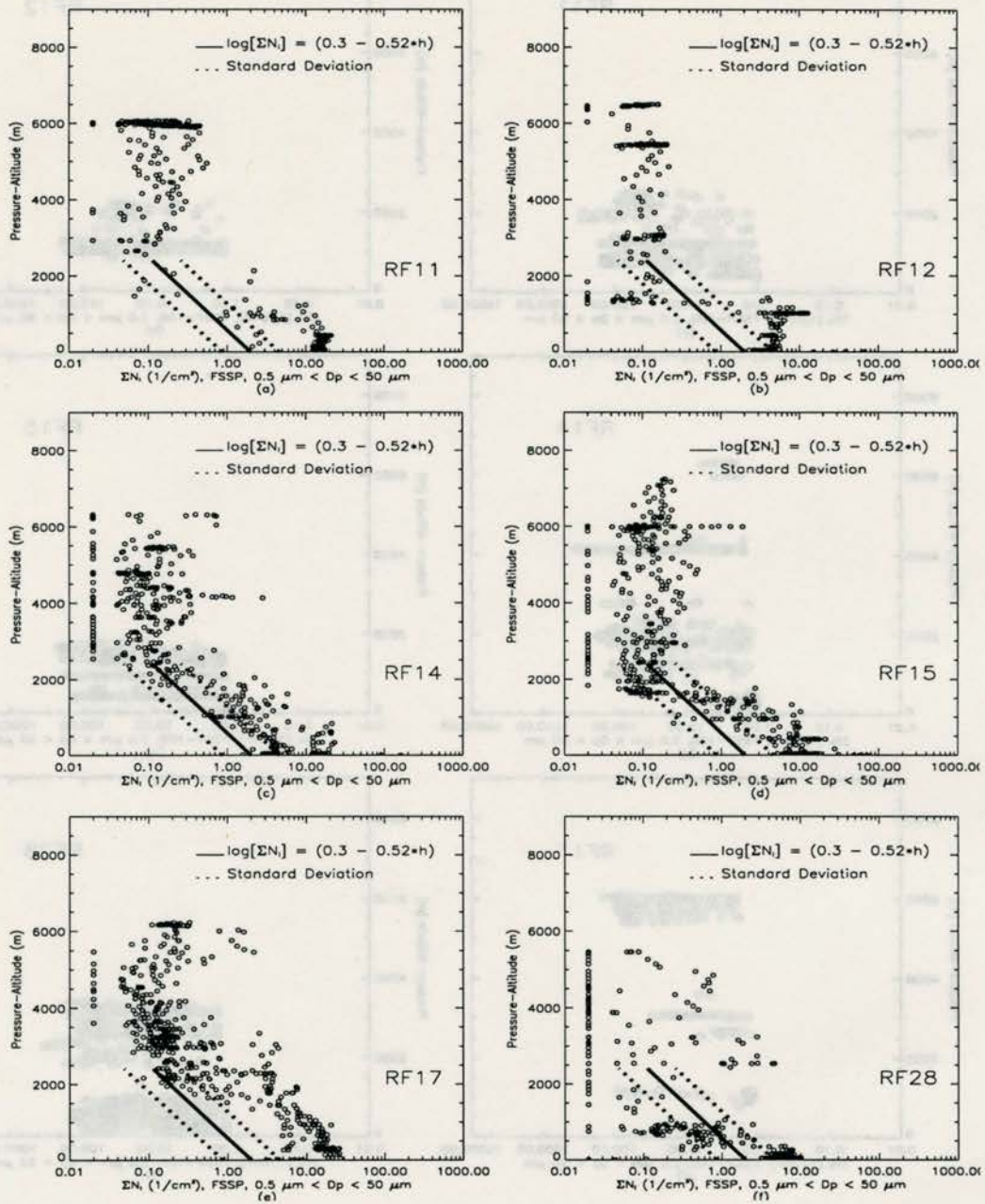


Figure 4.1.2 N_j concentrations as a function of altitude for the FSSP: a) RF 11, b) RF 12, c) RF 14, d) RF 15, e) RF 17, and f) RF 28. The solid line represents the fit, and the dashed line is standard deviation.

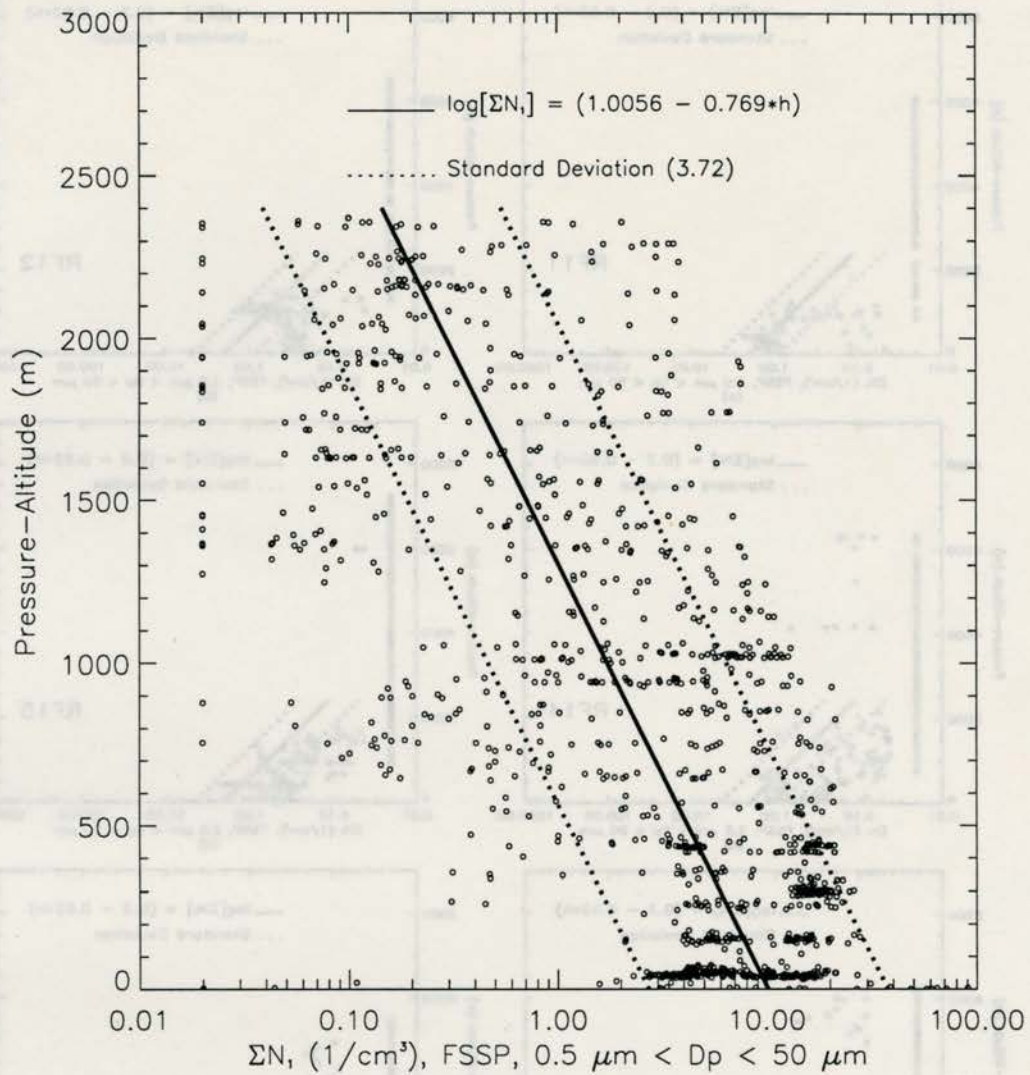


Figure 4.1.3 N_i concentrations for all flights as a function of altitude (for particle sizes of $0.5 \leq D_p \leq 50 \mu\text{m}$). The solid line represents the fit, and the dashed line represents the standard deviation.

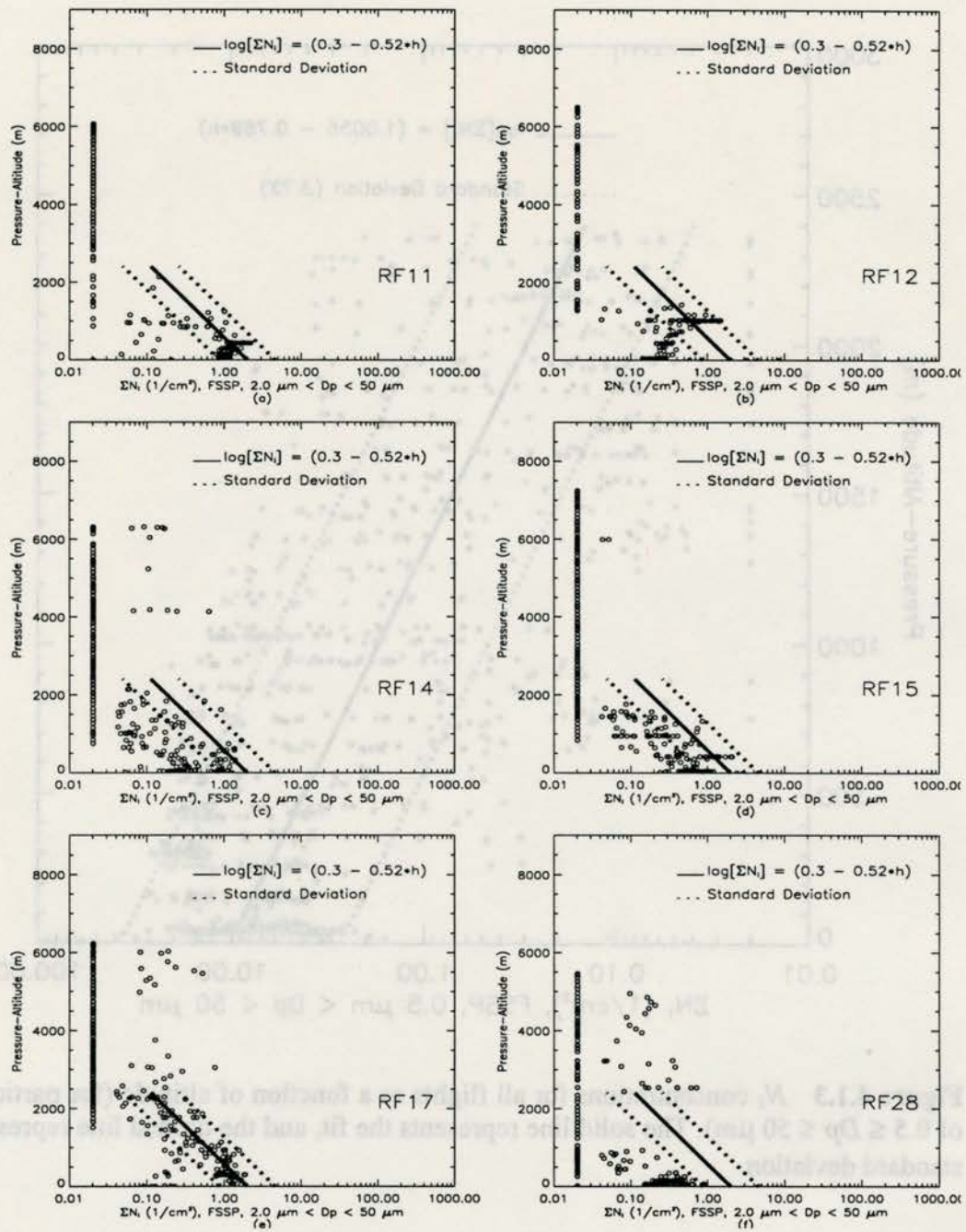


Figure 4.1.4 N_2 concentrations as a function of altitude for the FSSP: a) RF 11, b) RF 12, c) RF 14, d) RF 15, e) RF 17, and f) RF 28. The solid line represents the fit, and the dashed line represents the standard deviation.

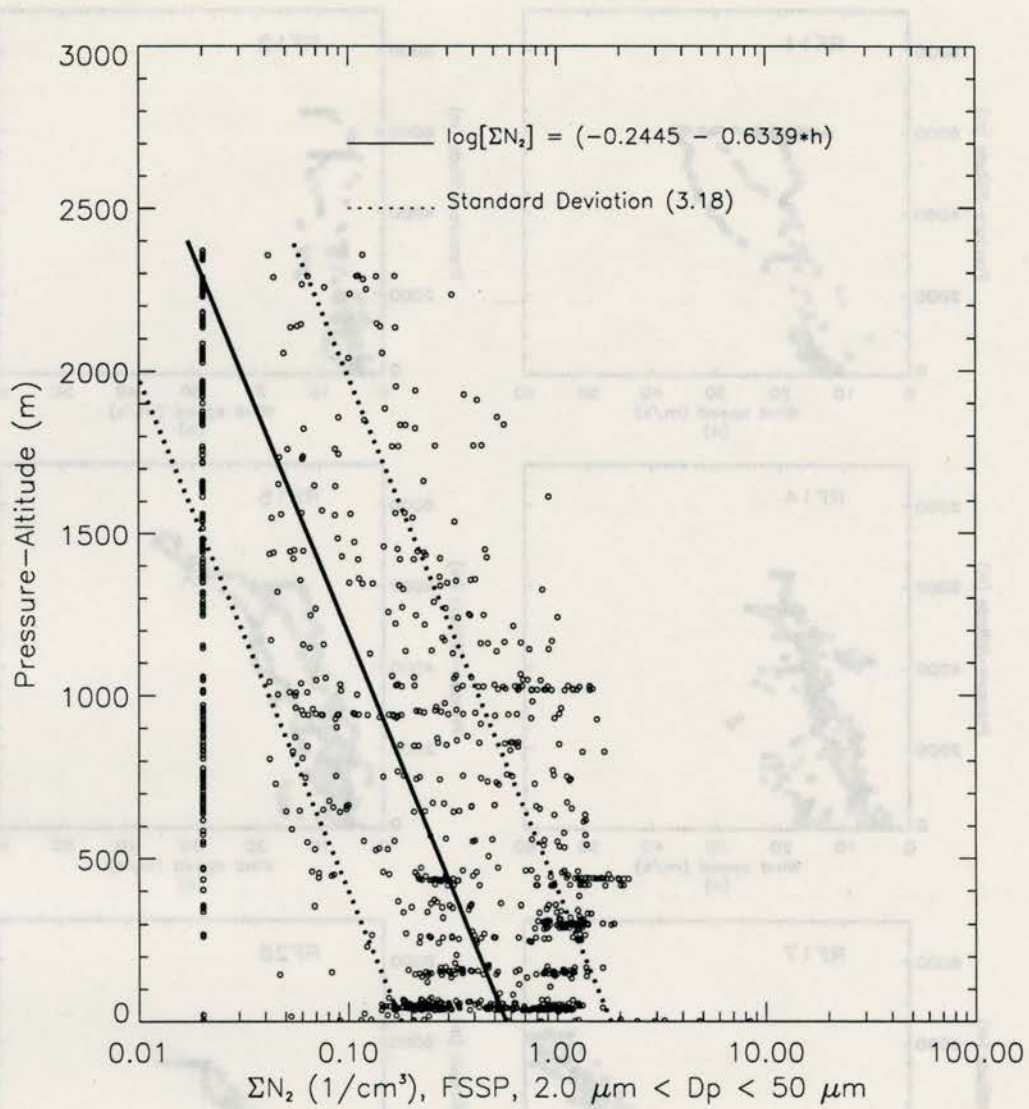


Figure 4.1.5 N_2 concentrations for all flights as a function of altitude (for particle sizes of $2.0 \leq D_p \leq 50 \mu\text{m}$). The solid line represents the fit, and the dashed line represents the standard deviation.

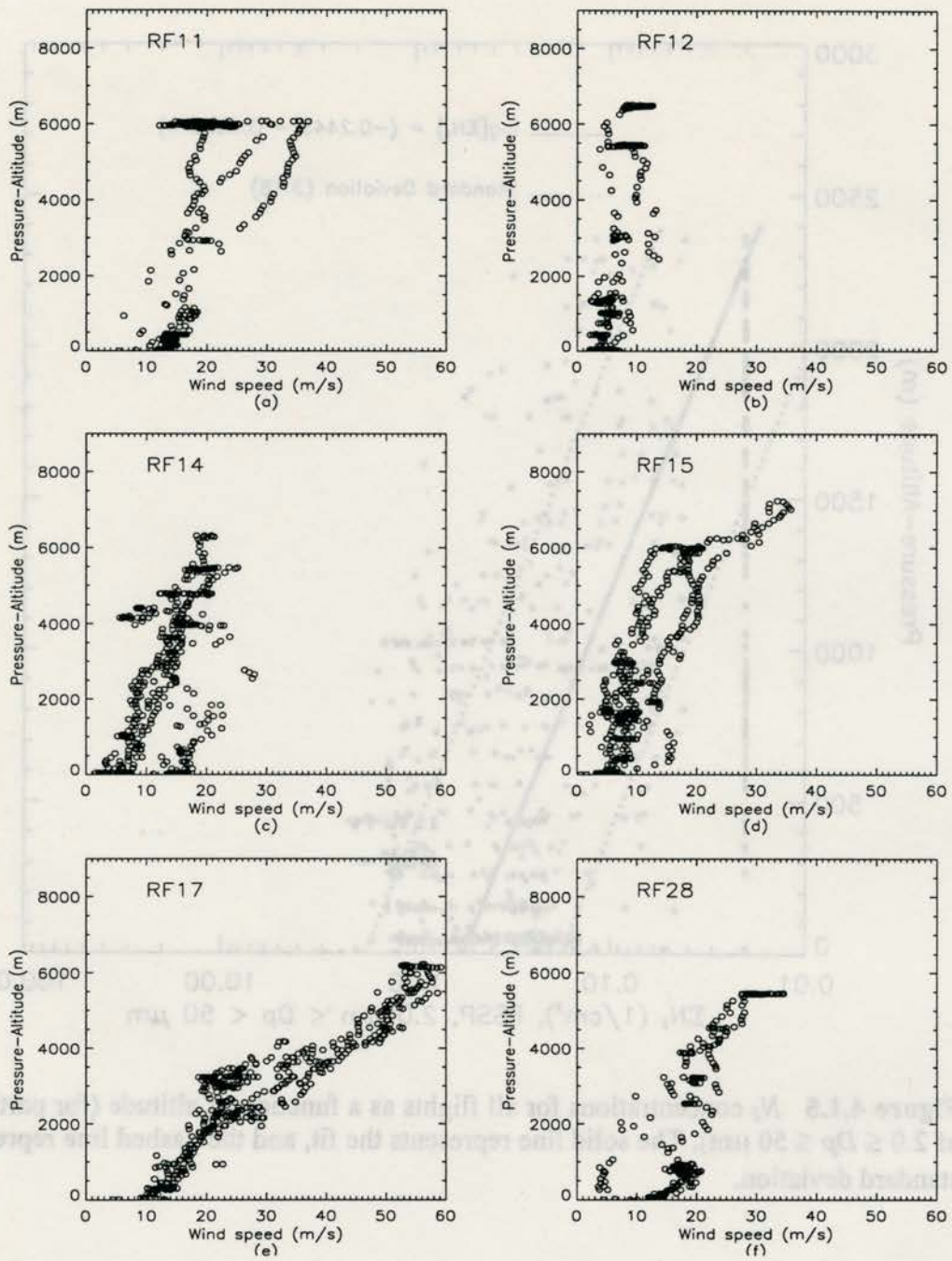


Figure 4.1.6 Vertical profiles of wind speed for each flight: a) RF 11, b) RF 12, c) RF 14, d) RF 15, e) RF 17, and f) RF 28.

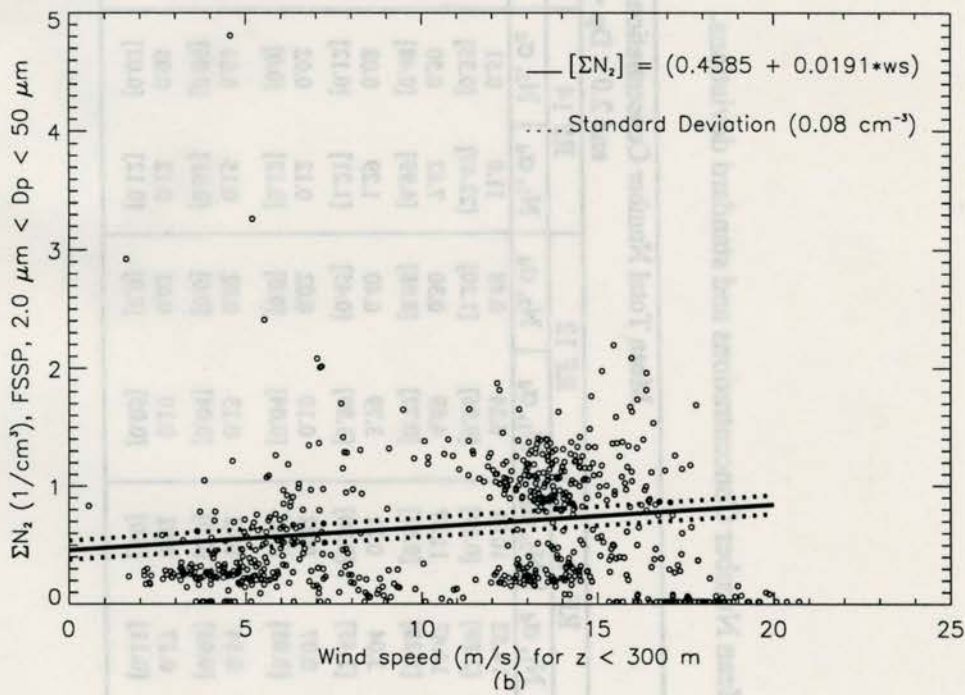
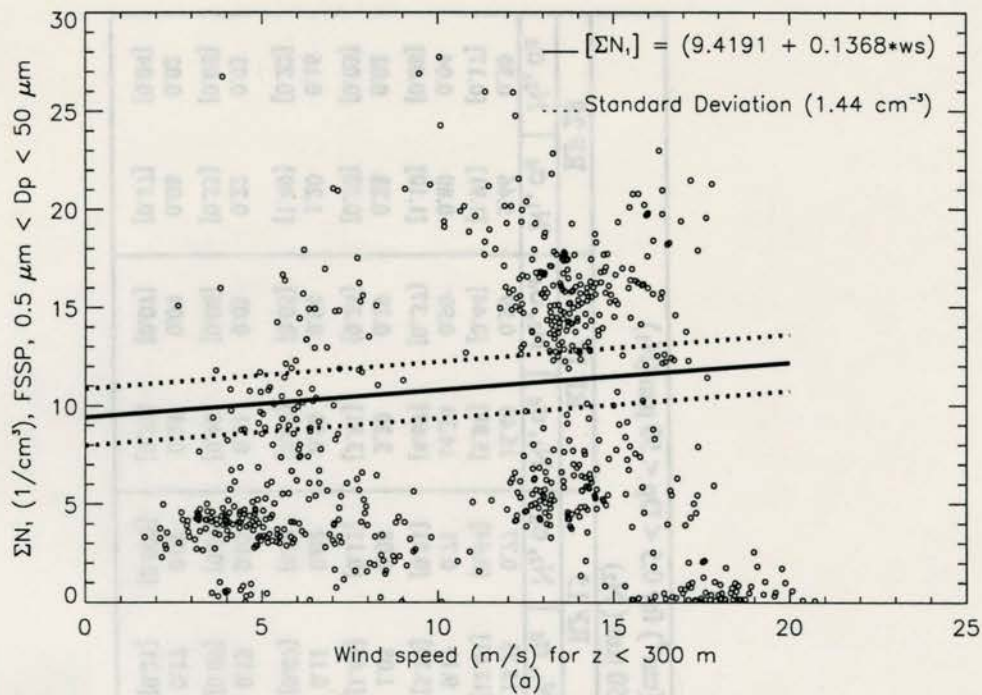


Figure 4.1.7 $[\Sigma N_1]$ and $[\Sigma N_2]$ concentrations as a function of wind speed for all flights. For a), the circles represent $[\Sigma N_1]$, and the solid line is the fit. For b), the circles represent $[\Sigma N_2]$, and the solid line is the fit. The dashed lines in both a) and b) are standard deviations.

Table 4.1.1 Mean Number Concentrations and standard deviations.

Altitude Layer	Mean Total Number Concentrations (cm^{-3}) for $0.5 < D_p < 50 \mu\text{m}$ (N_1) and $2.0 < D_p < 50 \mu\text{m}$ (N_2)											
	RF 11		RF 12		RF 14		RF 15		RF 17		RF 28	
	N_1, σ_d	N_2, σ_d	N_1, σ_d	N_2, σ_d	N_1, σ_d	N_2, σ_d	N_1, σ_d	N_2, σ_d	N_1, σ_d	N_2, σ_d	N_1, σ_d	N_2, σ_d
30 – 300 m	14.52 [2.89]	10.01 [0.27]	6.24 [9.96]	0.48 [1.20]	11.0 [22.47]	0.51 [0.35]	13.73 [12.61]	0.77 [0.64]	16.40 [5.88]	0.99 [0.44]	5.46 [1.91]	0.30 [0.17]
300 – 900 m	14.47 [5.28]	11.87 [0.52]	4.69 [0.72]	0.30 [0.08]	7.62 [6.99]	0.50 [0.48]	9.19 [5.15]	0.71 [0.51]	14.34 [4.69]	0.90 [0.37]	0.80 [1.10]	0.04 [0.08]
900 – 2400 m	3.04 [3.45]	0.21 [0.30]	3.79 [3.89]	0.40 [0.45]	1.29 [1.21]	0.08 [0.12]	1.08 [1.65]	0.08 [0.13]	3.30 [3.81]	0.19 [0.26]	0.28 [0.50]	0.02 [0.03]
2400 – 3000 m	0.07 [0.03]	0.02 [0.0]	0.10 [0.04]	0.02 [0.0]	0.12 [0.12]	0.02 [0.0]	0.11 [0.07]	0.02 [0.0]	0.50 [0.87]	0.04 [0.05]	1.20 [1.49]	0.16 [0.22]
3000 – 4250 m	0.14 [0.08]	0.02 [0.0]	0.13 [0.04]	0.02 [0.0]	0.15 [0.31]	0.03 [0.06]	0.13 [0.09]	0.02 [0.0]	0.21 [0.40]	0.03 [0.06]	0.22 [0.53]	0.03 [0.08]
$z > 4250$ m	0.17 [0.11]	0.02 [0.0]	0.10 [0.05]	0.02 [0.0]	0.12 [0.12]	0.03 [0.02]	0.17 [0.21]	0.02 [0.003]	0.23 [0.33]	0.04 [0.07]	0.08 [0.17]	0.02 [0.04]

Table 4.1.2 Mean Surface Area Concentrations and standard deviations.

Altitude Layer	Mean Total Surface Area Concentrations ($\mu\text{m}^2 \text{cm}^{-3}$) for $0.5 < D_p < 50 \mu\text{m}$ (S_1) and $2.0 < D_p < 50 \mu\text{m}$ (S_2)											
	RF 11		RF 12		RF 14		RF 15		RF 17		RF 28	
	S_1, σ_d	S_2, σ_d	S_1, σ_d	S_2, σ_d	S_1, σ_d	S_2, σ_d	S_1, σ_d	S_2, σ_d	S_1, σ_d	S_2, σ_d	S_1, σ_d	S_2, σ_d
30 – 300 m	75.35 [18.53]	32.48 [9.19]	27.38 [44.74]	14.34 [37.08]	48.69 [72.84]	25.95 [64.74]	61.91 [49.66]	22.07 [17.64]	75.18 [28.64]	32.63 [13.33]	51.08 [38.95]	36.41 [34.99]
300 – 900 m	90.34 [38.29]	44.89 [23.52]	30.67 [36.0]	17.60 [35.41]	47.04 [59.43]	26.72 [50.94]	50.06 [29.63]	22.89 [16.52]	66.52 [24.71]	29.27 [12.28]	6.09 [10.41]	4.14 [7.55]
900 – 2400 m	26.09 [38.95]	17.27 [29.84]	94.62 [158.17]	84.27 [151.48]	18.32 [62.42]	15.15 [61.30]	9.69 [31.07]	6.93 [27.83]	14.09 [19.29]	5.81 [9.41]	1.93 [5.03]	1.60 [4.26]
2400 – 3000 m	0.13 [0.07]	0.51 [0.0]	0.20 [0.12]	0.51 [0.0]	0.26 [0.44]	0.51 [0.0]	0.20 [0.14]	0.51 [0.0]	4.47 [17.43]	3.71 [17.0]	35.89 [45.03]	32.56 [40.89]
3000 – 4250 m	0.22 [0.11]	0.51 [0.0]	0.23 [0.08]	0.51 [0.0]	8.59 [48.23]	8.76 [47.40]	0.22 [0.15]	0.51 [0.0]	7.09 [67.74]	7.12 [66.88]	16.83 [51.66]	16.53 [50.64]
$z > 4250$ m	0.26 [0.18]	0.51 [0.0]	0.15 [0.08]	0.51 [0.0]	4.37 [18.87]	4.63 [18.48]	0.57 [2.77]	0.80 [2.48]	8.22 [24.63]	8.19 [23.82]	8.47 [28.73]	8.72 [28.22]

Table 4.1.3 Mean Volume Concentrations and standard deviations.

Altitude Layer	Mean Total Volume Concentrations ($\mu\text{m}^3 \text{cm}^{-3}$) for $0.5 < D_p < 50 \mu\text{m}$ (V_1) and $2.0 < D_p < 50 \mu\text{m}$ (V_2)											
	RF 11		RF 12		RF 14		RF 15		RF 17		RF 28	
	V_1, σ_d	V_2, σ_d	V_1, σ_d	V_2, σ_d	V_1, σ_d	V_2, σ_d	V_1, σ_d	V_2, σ_d	V_1, σ_d	V_2, σ_d	V_1, σ_d	V_2, σ_d
30 – 300 m	35.80 [10.93]	27.26 [9.07]	13.01 [26.93]	10.67 [26.01]	51.18 [216.38]	47.20 [216.63]	25.83 [30.43]	17.74 [28.67]	39.37 [24.25]	31.37 [23.54]	77.0 [94.33]	74.14 [93.62]
300 – 900 m	59.83 [49.10]	50.46 [47.55]	45.87 [146.14]	43.33 [146.06]	48.46 [141.38]	44.58 [141.07]	27.67 [29.80]	22.27 [29.47]	32.69 [14.50]	25.68 [12.59]	8.37 [16.44]	8.12 [15.91]
900 – 2400 m	48.75 [98.86]	46.99 [97.48]	304.45 [604.87]	302.40 [603.69]	57.94 [260.21]	57.37 [260.02]	18.15 [94.57]	17.70 [94.03]	6.48 [12.94]	4.93 [11.30]	2.82 [11.70]	2.86 [11.61]
2400 – 3000 m	0.02 [0.01]	0.25 [0.0]	0.04 [0.03]	0.25 [0.0]	0.05 [0.10]	0.25 [0.0]	0.04 [0.03]	0.25 [0.0]	12.97 [73.81]	12.93 [73.75]	94.86 [121.71]	94.21 [120.94]
3000 – 4250 m	0.03 [0.02]	0.25 [0.0]	0.04 [0.02]	0.25 [0.0]	32.34 [181.41]	32.51 [181.21]	0.04 [0.03]	0.25 [0.0]	28.57 [295.04]	28.72 [294.85]	57.86 [200.10]	57.91 [199.89]
$z > 4250$ m	0.04 [0.03]	0.25 [0.0]	0.02 [0.02]	0.25 [0.0]	15.28 [69.30]	15.48 [69.18]	1.0 [7.98]	1.20 [7.92]	25.68 [80.98]	25.80 [80.79]	28.27 [99.33]	28.44 [99.20]

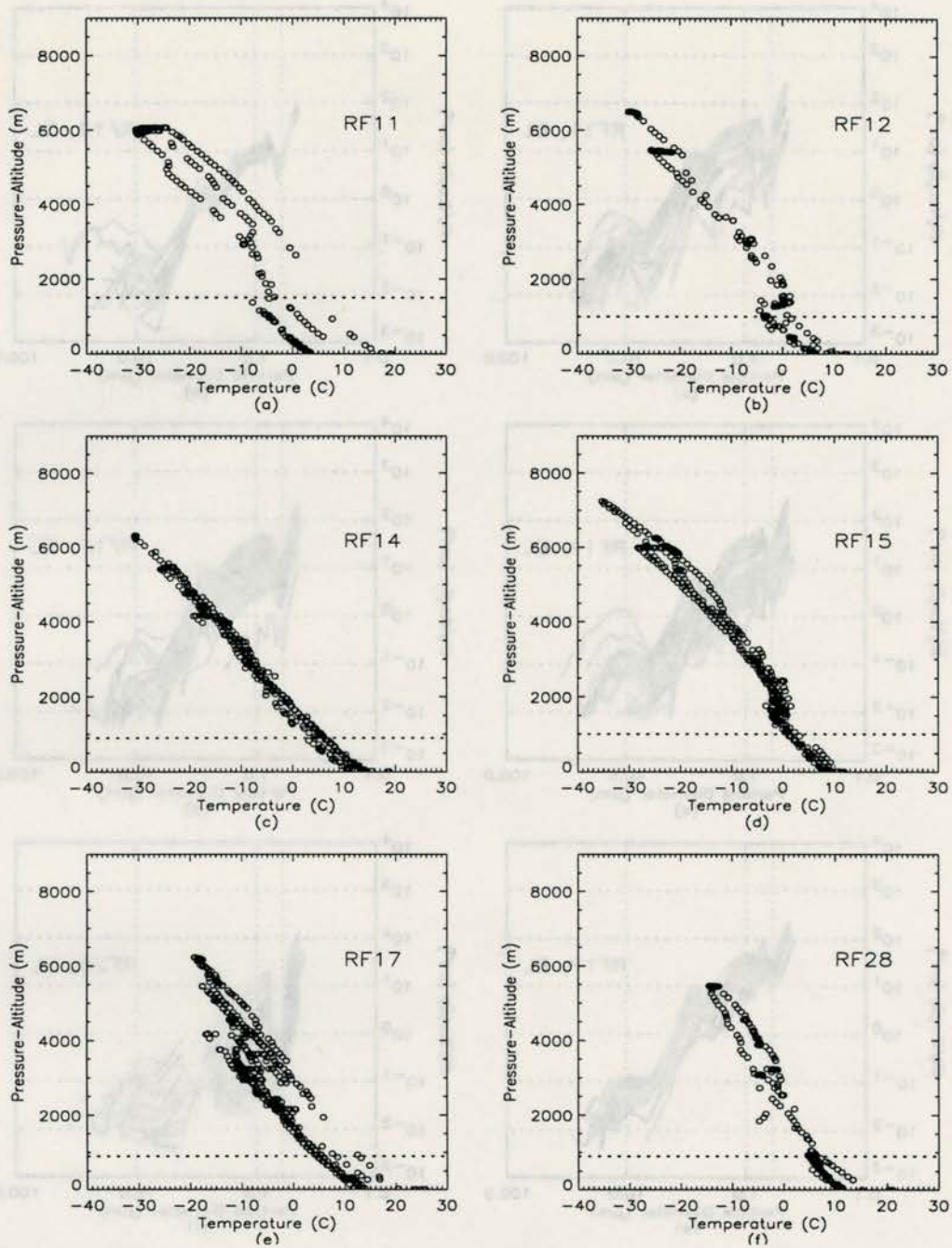


Figure 4.2.1 Vertical profiles of temperature for each flight: a) RF 11, b) RF 12, c) RF 14, d) RF 15, e) RF 17, and f) RF 28. The dashed line represents the inversion layer.

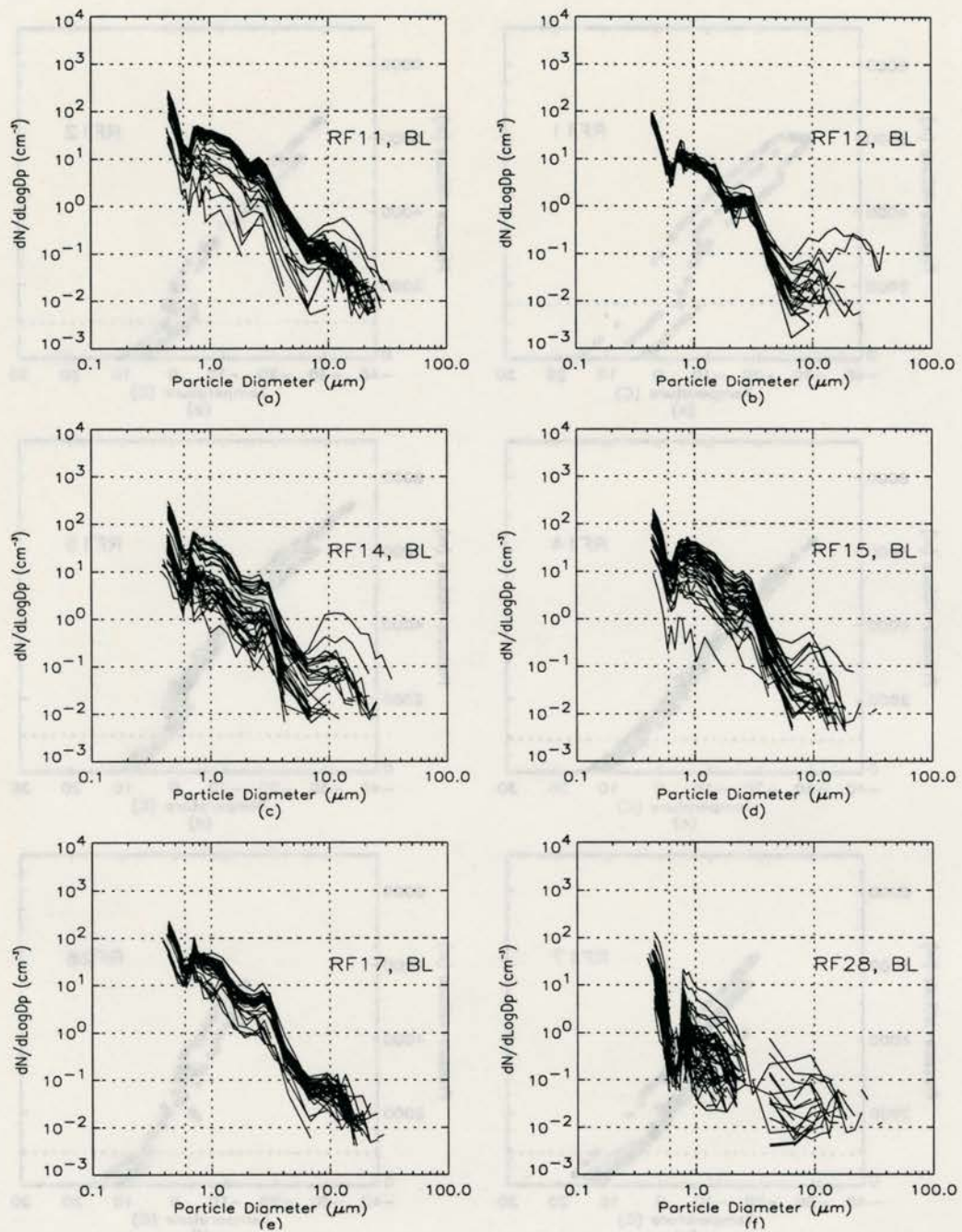


Figure 4.2.2 Size distributions for the boundary layer (300 to 900 m) for the FSSP (for particle size ranges $0.4 \leq D_p \leq 50 \mu\text{m}$): a) RF 11, b) RF 12, c) RF 14, d) RF 15, e) RF 17, and RF 28.

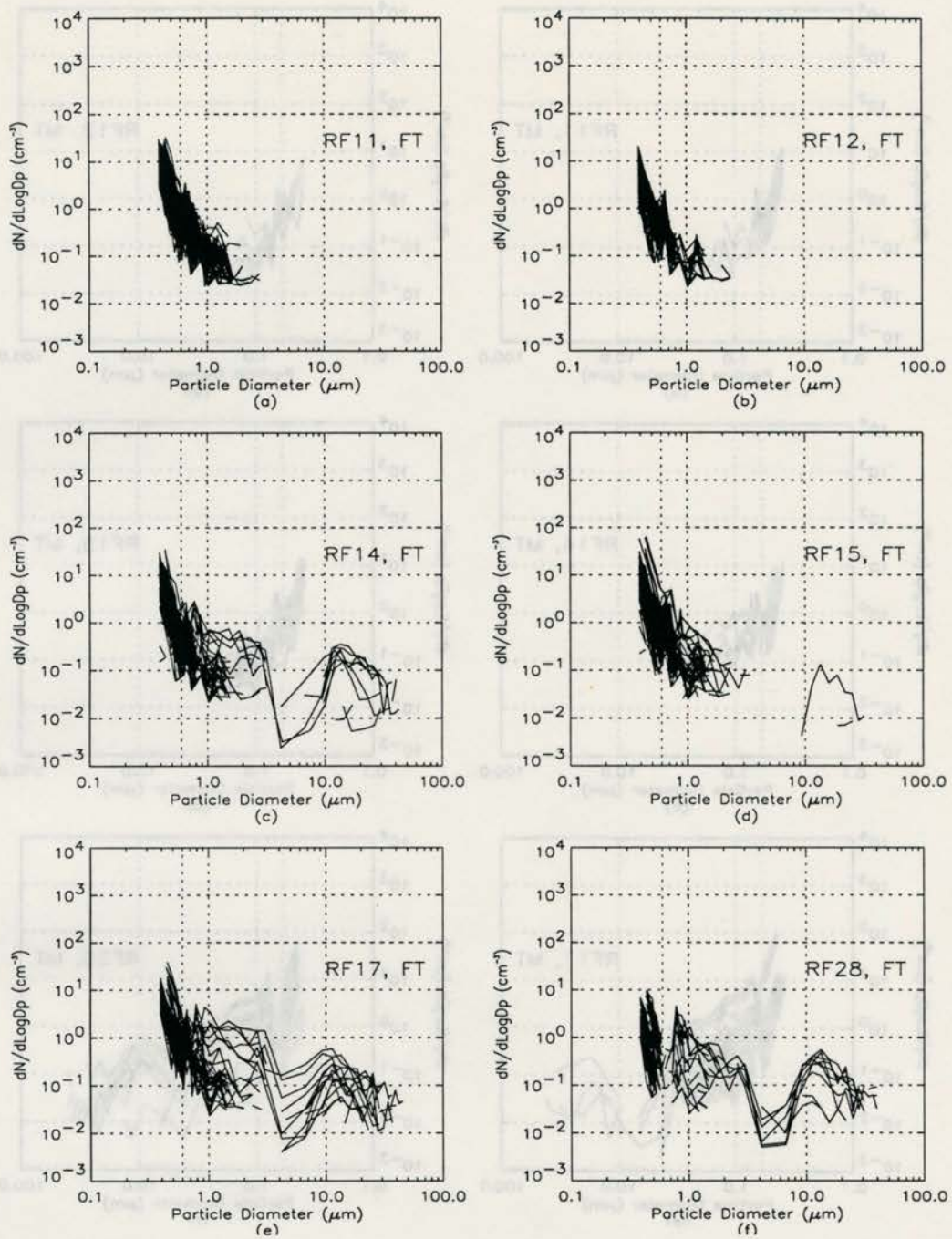


Figure 4.2.3 Size distributions for the mid troposphere (2400 to 3000 m) for the FSSP (for particle size ranges $0.4 \leq D_p \leq 50 \mu\text{m}$): a) RF 11, b) RF 12, c) RF 14, d) RF 15, e) RF 17, and RF 28.

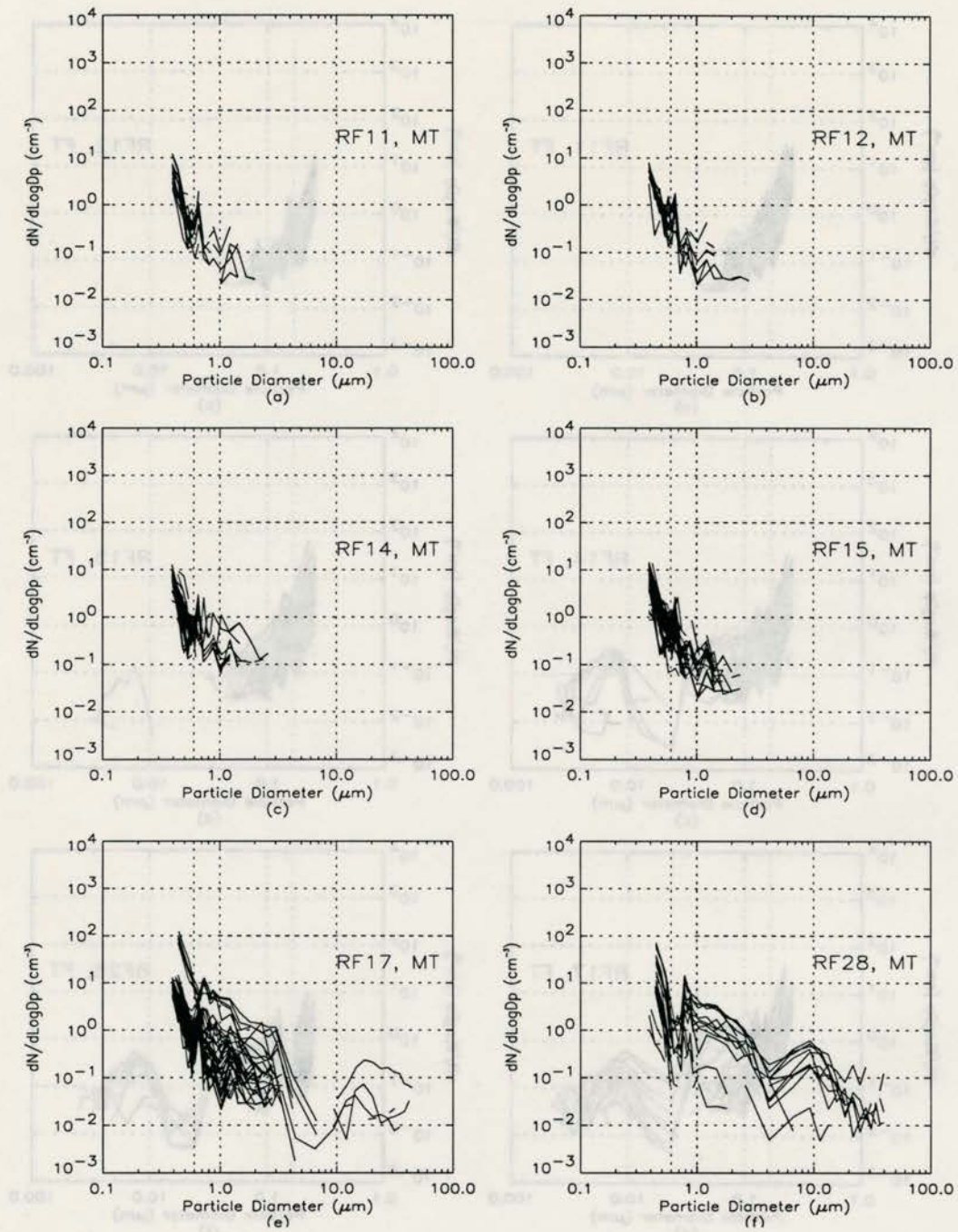


Figure 4.2.4 Size distributions for the free troposphere ($z > 4250$ m) for the FSSP (for particle size ranges $0.4 \leq D_p \leq 50 \mu\text{m}$): a) RF 11, b) RF 12, c) RF 14, d) RF 15, e) RF 17, and RF 28.

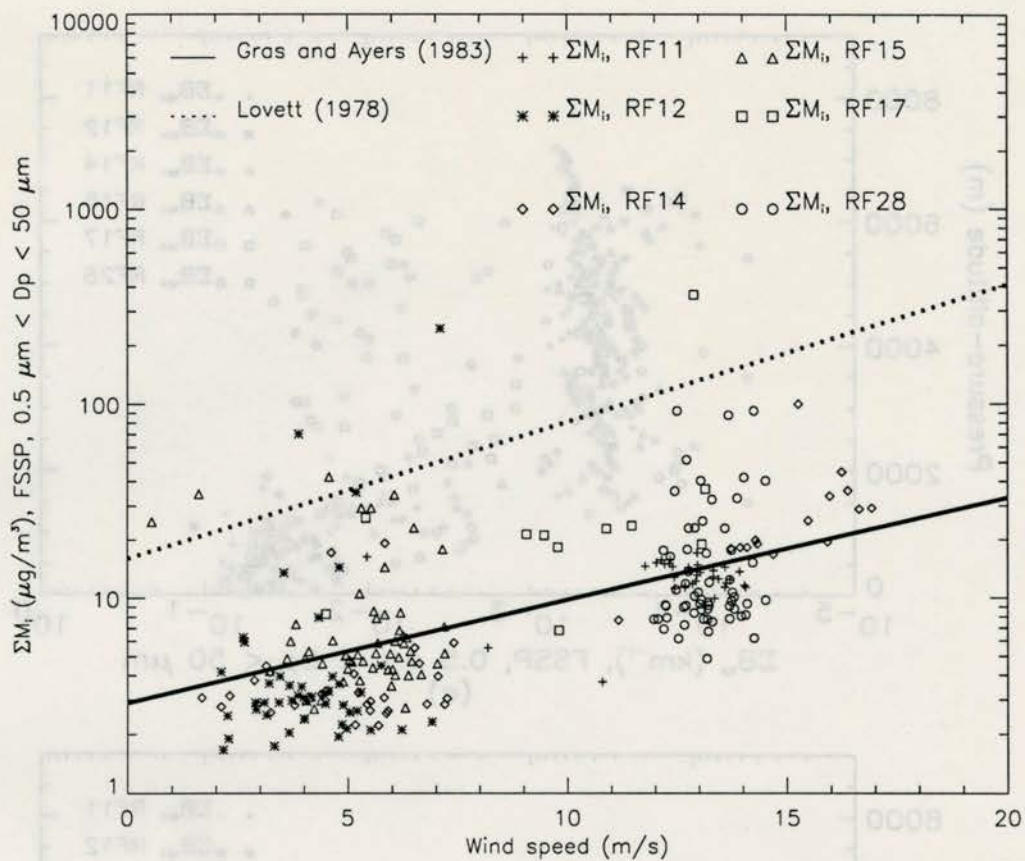


Figure 4.3.1 Dry sea salt mass concentrations as a function of wind speed for the FSSP (for particle size ranges $0.5 \leq D_p \leq 50 \mu\text{m}$): a) RF 11, b) RF 12, c) RF 14, d) RF 15, e) RF 17, and f) RF 28.

Table 4.3.1 Mean dry sea salt mass concentrations and standard deviations.

Altitude Layer	Mean Total Sea-salt Mass Concentrations ($\mu\text{g m}^{-3}$) for $0.5 < D_p < 50 \mu\text{m}$ (M_1)					
	RF 11	RF 12	RF 14	RF 15	RF 17	RF 28
	M_1, σ_d	M_1, σ_d	M_1, σ_d	M_1, σ_d	M_1, σ_d	M_1, σ_d
$z < 100 \text{ m}$	12.85 [2.69]	11.0 [36.46]	12.73 [17.16]	8.76 [8.94]	51.49 [98.77]	17.24 [19.34]

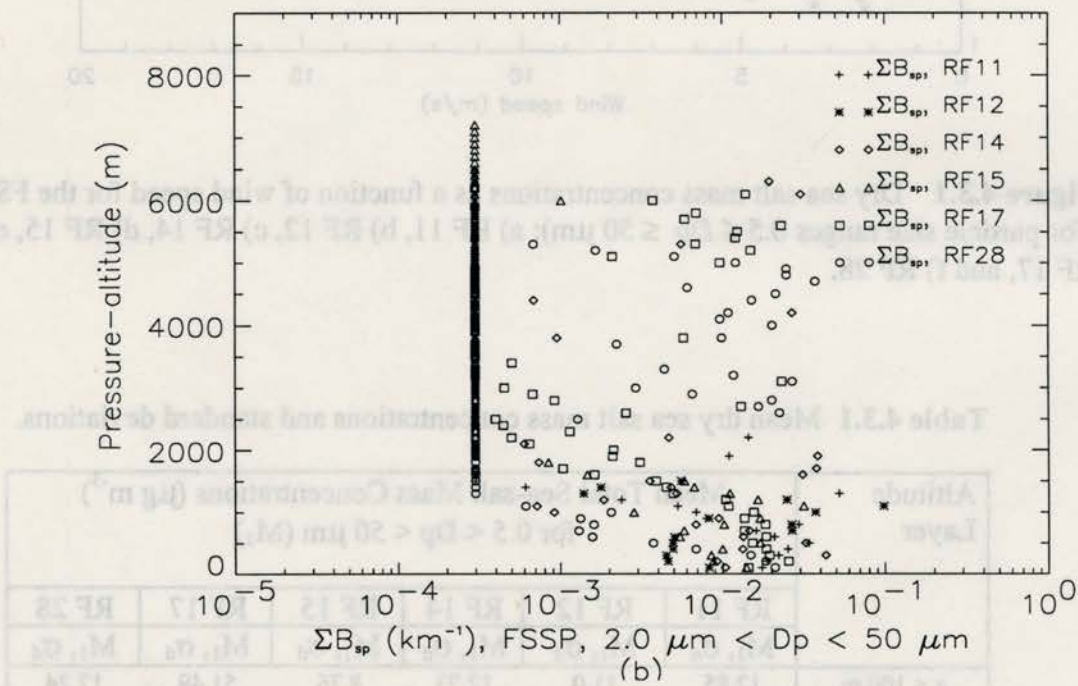
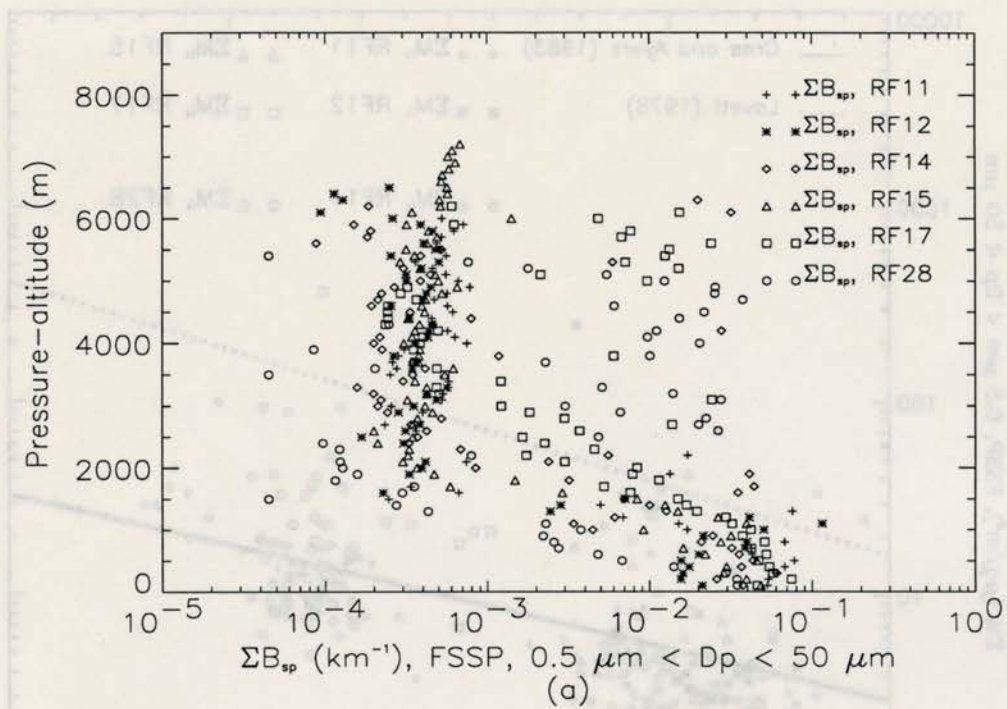


Figure 4.4.1 Mean ambient backscattering coefficient as a function of altitude for particle concentrations N_1 and N_2 . Each flight is represented by a certain symbol, which is shown on the graph.

Table 4.4.1 Contributions of aerosol research to optical properties.

Location	Instrumentation	Wavelength, λ	Total Light scattering Coefficient, Σb_{sp}
Coasts of California and Washington, C-131A research aircraft [Hegg <i>et al.</i> , 1996]	Three-wavelength backscatter nephelometer, $0.01 < D_p < 3.0 \mu\text{m}$	550 nm	$0.001 - 0.002 \text{ km}^{-1}$ ($200 < z < 350 \text{ m}$) and $0.0005 - 0.0009 \text{ km}^{-1}$ ($400 < z < 900 \text{ m}$)
Calculations to determine optical properties for a layer of sea salt [Winter and Chylek, 1997]	No instrumentation, $0.1 \leq D_p \leq 1.0 \mu\text{m}$, $r_o = 0.4 \mu\text{m}$, $\ln \sigma = 0.3$, $N = 20 \text{ cm}^{-3}$	550 nm	0.075 km^{-1} (for 75% RH) and 0.12 km^{-1} (for 80% RH) at $z < 1000 \text{ m}$
Aerosol Characterization Experiment (ACE-1), C-130 research aircraft [Baumgardner and Clarke, 1998]	Forward Scattering Spectrometer Probe (FSSP-300), $0.3 < D_p < 20 \mu\text{m}$	550 nm	$0.017 - 0.042 \text{ km}^{-1}$ ($z < 700 \text{ m}$) and 0.002 km^{-1} ($900 < z < 915 \text{ m}$)
Aerosol Characterization Experiment (ACE-1), Discoverer Ship [Quinn <i>et al.</i> , 1998]	Shipboard nephelometer with upstream impactors $D_{p_{aero}} < 1 \mu\text{m}$ $1.0 < D_{p_{aero}} < 10 \mu\text{m}$	550 nm	Submicron: $0.00066 - 0.038 \text{ km}^{-1}$ (average $0.0044 \pm 0.003 \text{ km}^{-1}$) Supermicron: $0.0017 - 0.13 \text{ km}^{-1}$ (average $0.023 \pm 0.016 \text{ km}^{-1}$)
Cape Grim Baseline Air Pollution Station (CGBAPS) [Carrico <i>et al.</i> , 1998]	Integrating nephelometer, $D_p < 10 \mu\text{m}$	550 nm	0.0148 km^{-1}
Mid-Atlantic Region of the eastern United States, C-131A research flight [Remer <i>et al.</i> , 1998]	Integrating nephelometer, $0.3 < D_p < 3 \mu\text{m}$	450 nm	$0.09 - 0.15 \text{ km}^{-1}$ ($z \leq 1000 \text{ m}$), peak values at 0.24 km^{-1} ($z \sim 1500$), and level off at 0.012 km^{-1} ($z \sim 2000 \text{ m}$), and above 2000 m values were $\sim 0.01 \text{ km}^{-1}$

Table 4.4.2 Optical depths computed from FSSP data ($z \leq 7000$ m).

Dp ranges	τ (RF 11)	τ (RF 12)	τ (RF 14)	τ (RF 15)	τ (RF 17)	τ (RF 28)
$0.5 \leq Dp \leq 50 \mu\text{m}$	0.066	0.044	0.059	0.043	0.085	0.048
$2.0 \leq Dp \leq 50 \mu\text{m}$	0.030	0.027	0.038	0.019	0.038	0.039

CHAPTER 5. DISCUSSION

Section 5.1. Particle lifetimes

There must be mechanisms that transport the observed large particles to higher altitudes. In this work, we assume these particles are entirely composed of sea salt. Sea salt particles are formed from the wave breaking mechanisms induced by winds at the surface of the ocean (Gong *et al.*, 1997). Once in the atmosphere, they can be transported upward by cyclonic / anticyclonic circulations (frontal zones), mixing and cloud processing, and deep convection (Covert *et al.*, 1996). The free troposphere is also a source of particles to the marine boundary layer, via transport by regional-scale or mesoscale subsidence (Bates *et al.*, 1998). Particles with $D_p > 10 \mu\text{m}$ have high gravitational settling velocities ($v_g \sim 80 \text{ cm s}^{-1}$ for $D_p \sim 10 \mu\text{m}$ and $v_g \sim 150 \text{ cm s}^{-1}$ for $D_p \sim 50 \mu\text{m}$) and therefore relatively short characteristic lifetimes (Prospero *et al.*, 1983; Jaenicke, 1988). Assuming particles are mixed throughout the depth of BL, lifetimes against removal by dry deposition range from weeks for particles with $D_p \sim 1 \mu\text{m}$, to ~ several days and ~ several hours for $D_p \sim 10$ and $50 \mu\text{m}$, respectively. Therefore, the largest of the particles are probably not attributable to long-range transport, but rather must have been fairly recently injected. At higher altitudes, the overall lifetime for $\sim 1 \mu\text{m}$ particles increases, but that for particles in the $10 - 50 \mu\text{m}$ size range is not substantially altered, since it is dominated by sedimentation (Jaenicke, 1988). Thus particles with $D_p > 10 \mu\text{m}$ must also have been injected into the MT and FT fairly

recently, probably by convective clouds. This hypothesis is supported by the observations of high N_2 in the MT and FT primarily in those flight missions and at those altitudes in which convective clouds were encountered.

Hygroscopic growth is also important in establishing the number concentrations of N_2 aerosols, since some of these particles may result from the growth of smaller particles under high-RH conditions. In areas of deep convection, cloud outflow could contribute to significant concentrations of both small and large particles by resuspension of particles from evaporating drops. The relatively high RH in cloud outflow and cloud dissipation regions could ensure that significant water mass remains in the aerosol phase.

We explored the relationship between RH and N_2 by generating scatter plots of these two quantities for different altitude levels. Figure 5.1.1 shows $\log[\sum N_2]$ as a function of relative humidity. The linear fit to $\log \sum N_2$ vs. RH was

$$\log[\sum N_2] = -1.7516 + 0.0126RH \quad (5.5.1)$$

Excluding values below the detection limit resulted in a positive correlation for altitudes above the BL ($r^2 \cong 0.3$). Above 2400 m, $N_2 > 0.05 \text{ cm}^{-3}$ was usually associated with RH > 60%, which is relatively moist for those levels of the troposphere. These observations support the association of large particles in the MT and FT with convective cloud transport. Despite their low concentrations, the abundance of > 2 μm particles is often sufficient to influence cloud microphysics, particularly drizzle formation (Feingold *et al.*, 1998).

Section 5.2. Effects of assumptions regarding aerosol water content

In this work, for purposes of determining the dry sea salt aerosol mass, it was assumed that particles existed in metastable equilibrium with the ambient RH, that is, they had been in equilibrium with RHs higher than the deliquescence RH and were following the efflorescence branch of the growth curve. This assumption may not be valid for particles that had been dried to low RH before being reintroduced to the BL. For data points with $46\% < \text{RH} < 74\%$, the range over which the hysteresis is observed, the mass fraction of water ranges from ~ 0.55 – 0.75 , shown in Figure 3.4.1. By removing this water content from the estimated aerosol mass concentration, we may have correspondingly underestimated sea salt mass concentrations. For four research flights (RF 11, RF 14, RF 15, and RF 17), a significant portion (50 – 100 %) of particles were found within the $46\% < \text{RH} < 74\%$ for $z < 100$ m. For RF 12 and RF 28, $\sim 2.1\%$ of particles were found within that RH range for $z < 100$ m. Referring back to Figure 4.3.1 in Chapter 4, mass concentrations ranging from $1 \mu\text{g m}^{-3}$ to $30 \mu\text{g m}^{-3}$ as a function of wind speed would have been underestimated by more than half. However, our methodology can also overestimate aerosol mass. Although submicron particles respond fairly quickly to fluctuations in ambient RH, this time constant is much slower (on the order of minutes) for $D_p > 10 \mu\text{m}$. Figure 5.2.1 shows the growth of an aerosol size distribution under constant supersaturation of 1% (Seinfeld and Pandis, 1998). The rate of growth of droplets is inversely proportional to their diameters so smaller droplets grow faster than larger ones. Evaporation of water from particles shows the same size dependence. Therefore, particles associated with evaporating cloud droplets may have

higher water contents than predicted by equilibrium, if they have been sampled soon after

cloud dissipation.

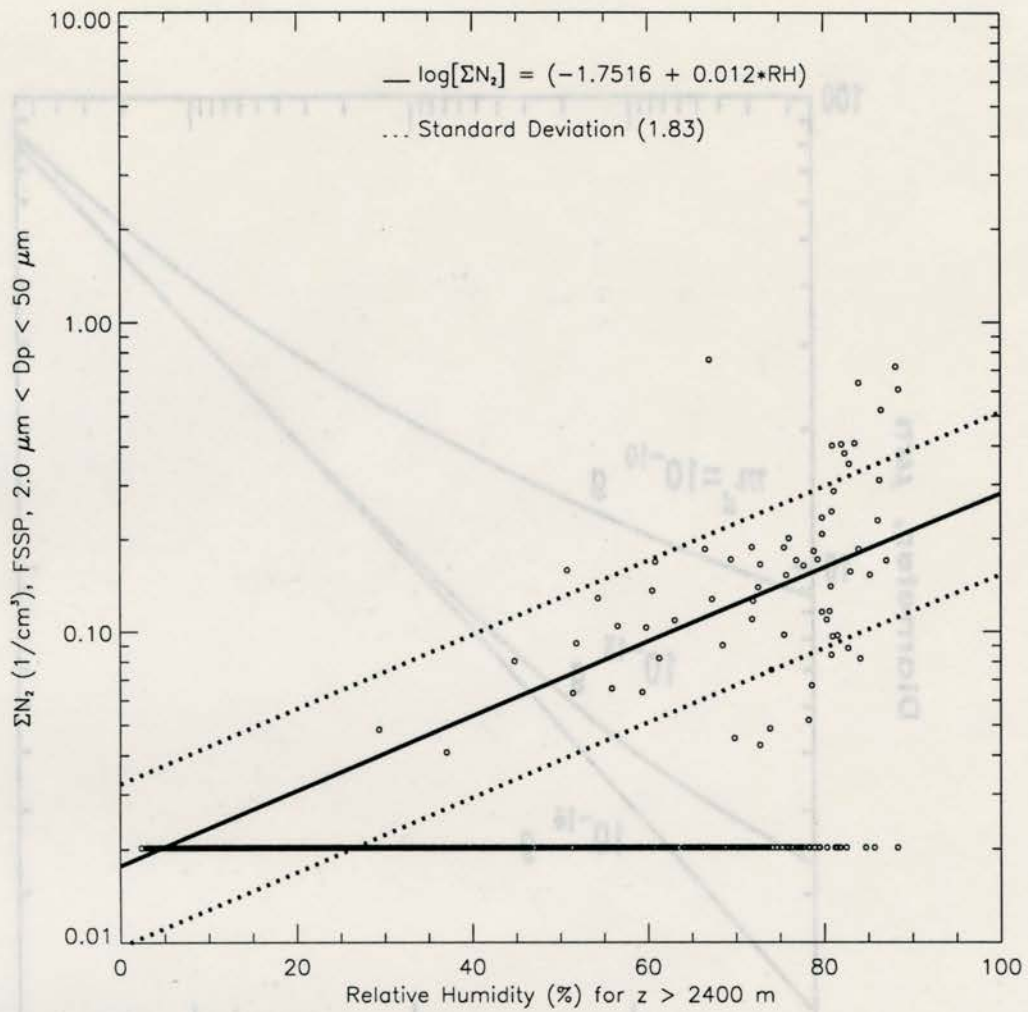


Figure 5.1.1 N_2 concentrations as a function of relative humidity (RH) for all flights. The circles represent N_2 , the solid line represents the fit, and the dashed lines are the standard deviation. The fit corresponds to N_2 concentrations above the average *LDL*.

Figure 5.1.1 Diffusional growth of individual drops with different dry masses as a function of time. The drops are initially at equilibrium at 80% RH (reproduced without permission from Seinfeld and Pandis, 1998)

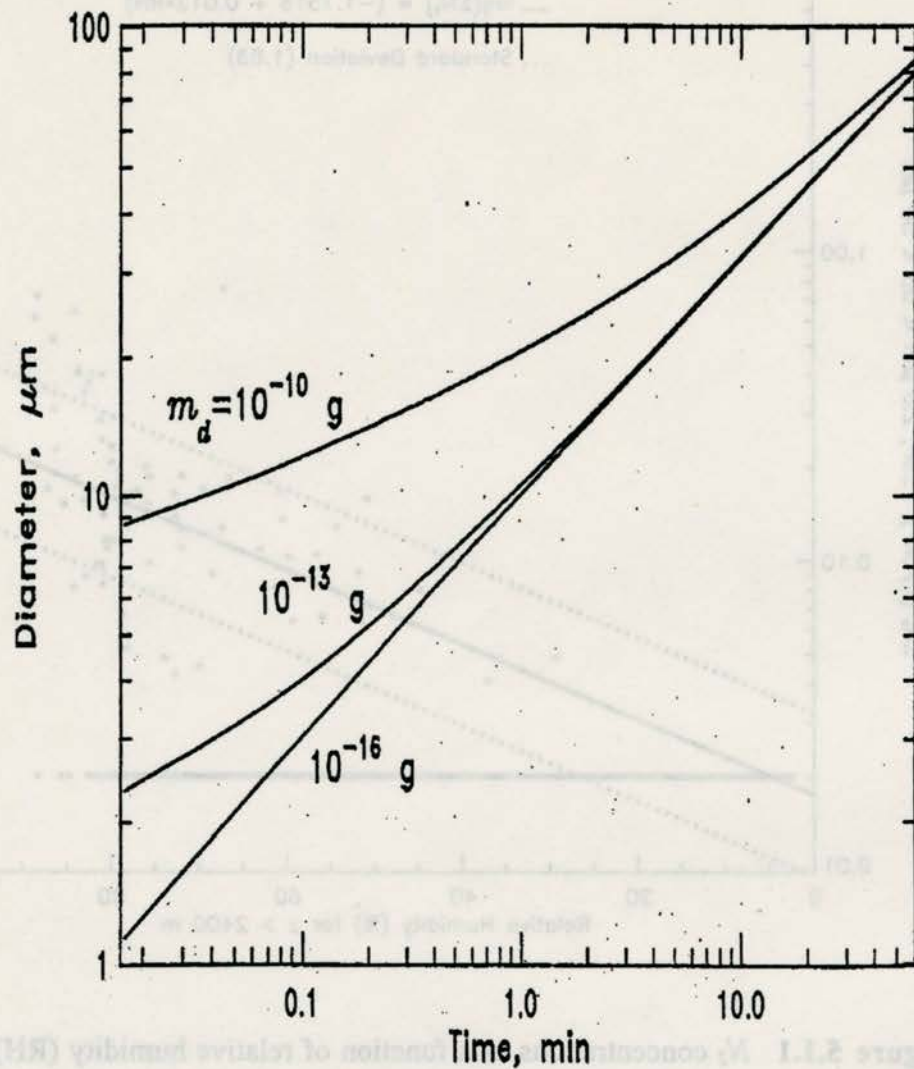


Figure 5.2.1 Diffusional growth of individual drops with different dry masses as a function of time. The drops are initially at equilibrium at 80% RH (reproduced without permission from Seinfeld and Pandis, 1998).

Figure 5.2.1 Diffusional growth of individual drops with different dry masses as a function of time. The drops are initially at equilibrium at 80% RH (reproduced without permission from Seinfeld and Pandis, 1998).

CHAPTER 6. SUMMARY AND CONCLUSIONS

The physical and optical characteristics of large particles ($D_p > 0.5 \mu\text{m}$ and $D_p > 2 \mu\text{m}$) over marine regions in the vicinity of Hobart, Tasmania have been examined, particularly their variation with altitude. Our analyses of data from 6 ACE-1 research flights suggest that deep convection, cloud outflow, and cloud dissipation strongly influence the concentrations of large particles in the mid- and free-troposphere. In the boundary layer, number concentrations of particles with $D_p \sim 10 \mu\text{m}$ appear to be most closely associated with local generation processes related to wind speed. This conclusion is supported by the observation that aerosol mass concentrations, assumed to be entirely sea salt, conformed to previously-published correlations with wind speed that were obtained using more traditional chemical measurements. The vertical variation of large aerosol number concentrations for $z < 2400 \text{ m}$ was similar to that observed by Kristament *et al.* (1993) near New Zealand, although the average number concentrations observed in the ACE-1 data were higher. The data set used here was for the spring / early summer season, whereas the New Zealand data covered all seasons; it is possible that seasonal variations in generation and transport mechanisms play a role. In particular, the ACE-1 study was conducted at latitudes known as the “roaring forties” and in a season associated with strong winds and sea-to-air fluxes.

The number size distributions also varied considerably with height, and between research flights. In the BL, the size distribution for RF 28 was suppressed for $D_p < 1 \mu\text{m}$.

This suppression could be attributed to depletion by drizzle in that case. The number size distributions and estimates of particle refractive index were used to compute light scattering coefficients and optical depths. The results showed that scattering by particles with $D_p > 2 \mu\text{m}$ could be a significant contribution to the scattering by all particles with $D_p > 0.5 \mu\text{m}$, particularly in the mid- and free troposphere for those cases where convection is suspected to play a role in the vertical transport of large particles. The computed optical depths were lower than estimates found in the literature, not surprising since particles smaller than $0.5 \mu\text{m}$ were not included.

This work contributes to the data base of knowledge regarding the vertical abundance of large particles in the troposphere. Despite their low number concentrations, such particles can play significant roles in light extinction and in drizzle initiation. The absence of data from austral fall and winter makes it difficult to determine seasonal variability in tropospheric aerosol concentrations. Extending the description to other latitudes and seasons would be useful.

with strong winds and sea-to-air fluxes.

The number size distributions also varied considerably with height, and between research flights. In the BL, the size distribution for RP 28 was suppressed for $D_p < 1 \mu\text{m}$.

CHAPTER 7. FUTURE WORK

The results reported within this study were limited to the early austral spring (December and November in the Southern Hemisphere). It would be most beneficial to include vertical profiles of large aerosols during other seasons in order to determine seasonal variability in aerosol profiles and convective events that enhance large particle concentrations aloft. Within this study, only 6 research flights were evaluated, but there were a total of 33 flights. The other research flights should be evaluated for a more intensive study that includes data from other latitudes and longitudes as well. The data were also restricted to evaluating particles $> 0.5 \mu\text{m}$. It would also be useful to include the lower portion the particle spectra ($D_p < 0.5 \mu\text{m}$) when evaluating the contribution of the accumulation mode versus the coarse mode.

When developing the index of refraction tables, the particles were assumed to be composed entirely of sea salt and water. Other authors (Quinn *et al.*, 1998, Murphy *et al.*, 1998; Fitzgerald, 1991; Gras and Ayers, 1983) reported that sea salt comprised a large portion ($> 90 \%$) of total aerosol mass. Non-sea salt sulfate (nss SO_4^-) was found to contribute a minimum of $2 \pm 2 \%$ of the total aerosol mass and nss SO_4^- accounted for $2.5 \pm 2 \%$ of total scattering for the submicron particles ($D_p < 1.0 \mu\text{m}$, Quinn *et al.*, 1998). The small fraction of nss SO_4^- could be incorporated for a sensitivity study. Furthermore, it would be useful to study the effects of following the deliquescence branch instead of the efflorescence branch of the hygroscopicity curve.

Satellite observations (P. Durkee et al., manuscript in preparation) were made during ACE-1 at Cape Grim and Hobart baseline stations in Tasmania and on the C-130 aircraft. These measurements were used to report the aerosol optical properties within the study region. The aerosol optical properties calculated in this work should be compared to Durkee's work to determine if the values reported here are reasonable.

REFERENCES

- Bates, T. S., Huebert, B. J., Gras, J. L., Griffiths, F. B., and Durkee, P. A., 1998, International Global Atmospheric Chemistry (IGAC) Project's First Aerosol Characterization Experiment (ACE-1): Overview, *Journal of Geophysical Research*, **103**: 16297-16318.
- Baumgardner, D. and Clarke, A., 1998, Changes in Aerosol Properties with relative humidity in the remote Southern Hemisphere boundary layer, *Journal of Geophysical Research*, **103**: 16525-16534.
- Baumgardner, D., Dye, J. E., and Gandrud, B. W., 1992, Interpretation of measurements made by the forward scattering spectrometer probe (FSSP-300) during the Airborne Arctic Stratospheric Expedition, *Journal of Geophysical Research*, **97**: 8035-8046.
- Baumgardner, D., Dye, J. E., and Gandrud, B. W., 1989, Calibration of the forward scattering spectrometer probe used on the ER-2 during the airborne Antarctic Ozone Experiment, *Journal of Geophysical Research*, **94**: 16475-16480.
- Baumgardner, D., 1983, An analysis and comparison of five water droplets measuring instruments, *Journal of Climate and Applied Meteorology*, **22**: 891-910.
- Cerni, T. A., 1983, Determination of the size and concentration of cloud drops with an FSSP, *Journal of Climate and Applied Meteorology*, **22**, 1346-1355.
- Cerni, T. A. and Cooper, W. A., 1982, Conference on Cloud Physics, American Meteorological Society, Boston, Mass., 275-278.
- Clark, A. D., Varner, J. L., Eisele, F., Mauldin, R. L., Tanner, D., and Litchy, M., 1998, Particle production in the remote marine atmosphere: cloud outflow and subsidence during ACE-1, *Journal of Geophysical Research*, **103**: 16397-16409.
- Covert, D. S., Kapustin, V. N., Bates, T. S., and Quinn, P. K., 1996, Physical properties of marine boundary layer aerosol particles of the mid-Pacific in relation to sources and meteorological transport, *Journal of Geophysical Research*, **101**: 6919-6930.
- Dye, J. E. and Baumgardner, D., 1984, Evaluation of the Forward Scattering Spectrometer Probe. Part I: Electronic and Optical Studies, *Journal of Atmospheric and Oceanic Technology*, **1**: 329-344.
- Durkee, P. A., Pfiel, T., Frost, E., and Shewa, R., 1991, Global analysis of aerosol particle characteristics, *Atmospheric Environment*, **25A**: 2457-2471.
- Feingold, G., Cotton, W. R., Kreidenweis, S. M., and Davis, J. T., 1998, The impact of

giant CCN on Drizzle formation in stratocumulus: implications for cloud radiative properties, Submitted to *Journal of Atmospheric Science*.

Fitzgerald, J. W., 1991, Marine Aerosols: A Review, *Atmospheric Environment*, **25A**: 533-545.

Gong, S. L., Barrie, L. A., and Blanchet, J.-P., 1997, Modeling sea-salt aerosols in the atmosphere 1. Model development, *Journal of Geophysical Research*, **102**: 3805-3818.

Gras, J. L. and Ayers, G. P., 1983, Marine aerosol at Southern mid-latitudes *Journal of Geophysical Research*, **88**: 10661-10666.

Hegg, D. A., Covert, D. S., Rood, M. J., and Hobbs, P. V., 1996, Measurements of aerosol optical properties in marine air, *Journal of Geophysical Research*, **101**: 12,893-12,903.

Hegg, D., Larson, T., and Yuen, P., 1993, A theoretical study of the effect of relative humidity on light scattering by tropospheric aerosols, *Journal of Geophysical Research*, **98**: 18435-18439.

Hudson, J. G., Xie, Y., and Yum, S. S., 1998, Vertical distributions of cloud condensation nuclei spectra over the summertime Southern Ocean, *Journal of Geophysical Research*, **103**: 16609-16623.

Jaenicke, R., 1988, Langfristige Änderungen des Aerosols, *Promet*, **16**: 13-18.

Kristament, I. S., Liley, J., and Harvey, M., 1993, Aerosol variability in the vertical in the Southwest Pacific, *Journal of Geophysical Research*, **98**: 7129-7139.

Lovett, R. F., 1978, Quantitative measurement of airborne sea-salt in the North Atlantic, *Tellus*, **30**: 358-364.

Moelwyn-Hughes, E. A. 1961, *Physical Chemistry*, 2nd rev. ed., Pergamon, Tarrytown, New York.

Murphy, D. M., Anderson, J. R., Quinn, P. K., McInnes, L. M., Brechtel, F. J., Kreidenweis, S. K., Middlebrook, A. M., Posfai, M., Thompson, D. S., and Buseck, P. R., 1998, Influence of sea-salt on aerosol radiative properties in the Southern Ocean marine boundary layer, *Nature*, **392**: 62-64.

Norment, H. G., 1988, Three-Dimensional Trajectory Analysis of two drop sizing instruments: PMS* OAP and PMS* FSSP, *Journal of Atmospheric and Oceanic Technology*, **5**, 743-756.

Pinnick, R. G. and Auvermann, H. J., 1979, Response characteristics of Knollenberg

- light-scattering aerosol counters, *Journal of Aerosol Science*, **10**, 55-74.
- Pinnick, R. G., Garvey, D. M., and Duncan, L. D., 1981, Calibration of Knollenburg FSSP light-scattering counters for measurement of cloud droplets, *Journal of Applied Meteorology*, **20**: 1049-1057.
- Prospero, J. M., Charlson, R. J., Mohnen, V., Jaenicke, R., Delany, A. C., Moyers, J., Zollen, W., and Rahn, K., 1983, Atmospheric Aerosol System: An Overview, *Review of Geophysical Space and Physics*, **21**: 1607-1629.
- Pruppacher, H. R., and Klett, J. D., 1989, Microphysics of Clouds and Precipitation, D. Reidel, Norwell, Mass.
- Quinn, P. K., Coffman, D. J., Kapustin, V. N., and Bates T. S., 1998, Aerosol optical properties in the marine boundary layer during ACE-1 and the underlying chemical and physical aerosol properties, *Journal of Geophysical Research*, **103**: 16547-16564.
- Remer, L. A., Gasso', S., Hegg, D. A., Kaufman, Y. J., and Holben, B., 1997, Urban/industrial aerosol; ground-based sun/sky radiometer and airborne in situ measurements *Journal of Geophysical Research*, **102**: 16849 – 16859.
- Skoog, D. A., West, D. M., Holler, F. J., 1996, Fundamentals of Analytical Chemistry, Saunders College Publishing, Ft. Worth, TX.
- Tang, I. N., Tridico, A. C., and Fung, K. H., 1997, Thermodynamic and optical properties of sea salt aerosols *Journal of Geophysical Research*, **102**: 23269-23275.
- Toon, O. B. and Pollack, J. B., 1976, A global average model of atmospheric aerosols for radiative transfer calculations, *Journal of Applied Meteorological*, **15**: 225-246.
- Twomey, S., 1991, Aerosols, clouds and radiation, *Atmospheric Environment*, **25A**(11): 2435-2442.
- Winter, B. and Chylek, 1997, Contribution of sea salt aerosol to the planetary clear-sky albedo, *Tellus*, **49B**: 72-79.

light-scattering aerosol counter, *Journal of Aerosol Science*, 10, 55-74.

Frank, R. G., Govey, D. M., and Duceon, L. D., 1981, Calibration of Knollenburg TSSP light-scattering counter for measurement of cloud droplets, *Journal of Applied Meteorology*, 20: 1049-1057.

Propero, J. M., Chanson, R. J., Mahan, V., Jankovic, B., Delany, A. C., Meyer, J., Zoller, W., and Rahn, K., 1987, Atmospheric Aerosol System: An Overview, *Review of Geophysical Space and Physics*, 21: 1607-1620.

Proppacher, H. R., and Klein, J. D., 1989, *Micropysics of Clouds and Precipitation*, D. Reidel, Norwell, Mass.

Quinn, P. K., Colfinan, D. J., Kasparian, V. N., and Bates, T. S., 1998, Aerosol optical properties in the marine boundary layer during ACE-1 and the underlying chemical and physical processes, *Journal of Geophysical Research*, 103: 16547-16564.

Raman, L. A., Gamo, S., Hogg, D. A., Kaufman, Y. J., and Holbert, B., 1997, Urban/industrial aerosol: ground-based weekly radiances and airborne in situ measurements, *Journal of Geophysical Research*, 102: 16849 - 16859.

APPENDIX

Skoog, D. A., West, D. M., Holler, F. J., 1996, *Fundamentals of Analytical Chemistry*, Saunders College Publishing, Ft. Worth, TX.

Tang, I. N., Tishco, A. C., and Pong, K. H., 1997, Thermodynamic and optical properties of sea salt aerosols, *Journal of Geophysical Research*, 102: 23269-23272.

Toon, O. B. and Pollack, J. B., 1978, A global average model of atmospheric aerosols for radiative transfer calculations, *Journal of Applied Meteorology*, 17: 225-246.

Twomey, S., 1991, Aerosols, clouds and radiation, *Atmospheric Environment*, 25A(11): 2433-2442.

Winters, B. and Chylek, 1997, Contribution of sea salt aerosol to the planetary clear-sky albedo, *Science*, 275: 77-79.

APPENDIX

The Forward Scattering Spectrometer Probes (FSSP-100 and -300) are manufactured by Particle Measuring Systems (PMS Inc., Boulder, Co). The sensors were originally developed for the study of stratospheric aerosol distributions and polar stratospheric clouds, but now the sensors are widely utilized in studies of tropospheric chemistry and aerosols (Baumgardner and Dye, 1984). Part I of Appendix A explores the principle operation of the FSSPs more thoroughly than shown in Chapter 2.

Particle sizing as a function of light intensity, scattering angles, and refractive index are discussed in Part II of Appendix A. Other factors such as airspeed and flow distortions are included since these variables can affect particle sizing as well as particle concentrations.

Concentration corrections that were used for this study are also presented. Since the data were obtained as raw counts, particle concentrations had to be derived as functions of particle rate, true air speed, and sampling area of the FSSP-100 and the FSSP-300. Therefore, concentration and sizing uncertainties are discussed because most values affecting these parameters are approximated, which does not account for variations. Lower detection limit approximations are also discussed. This procedure is also done for surface area concentrations, volume concentrations, and total light scattering coefficient.

APPENDIX A.

Part I. Principles of operation of the FSSPs

The FSSP-100 and 300 are of the general class of instruments called optical particle counters (OPCs) that detect single particles and size them by measuring the intensity of light that the particle scatters when passing through a light beam (Dye and Baumgardner, 1984). The schematic diagram shown in Figure A1.1.1 illustrates the optical path of this instrument for the FSSP-100. A helium neon laser is focused to a small diameter at the center of an inlet that faces into the incoming airstream. The light that is scattered forward by particles passing through the beam is collected from a solid angle defined by the diameter of the dump spot and the collection optics. This light then passes through a prism and collecting lens and enters a beam splitting prism. One portion of the light from the prism illuminates a photodetector that is referred to as the signal detector, while the other portion falls on a photodetector that has been partially masked to detect only that light from $4 - 12^\circ$ (Dye and Baumgardner, 1984). This defines an annulus of scattered light. The output of both detectors are amplified and conditioned, with the output of the annulus typically amplified 2 to 3 times more than the signal. Particles passing through the beam far from the focal plane scatter proportionally more light into the annulus than those close to the focal plane. Therefore, the depth-of-field (*DOF*) can be established by an electronic comparison of the annulus and signal voltages. Once the signal is determined, the particle can be defined within certain channels by the pulse height analyzer (PHA), which is discussed further in Part II.

The FSSP-300 has a different working system than the FSSP-100. Figure A1.1.2 displays a diagram that is similar to the Figure A1.1.1, but the FSSP-300 uses a clear aperture and masked slit aperture system (Baumgardner *et al.*, 1992). The sample volume is fixed by comparing the simultaneous signal amplitudes observed at the two detectors, thus establishing a small region of “acceptance” within the optical field-of-view (Baumgardner *et al.*, 1992). The masked slit detector amplitude must be equal to or greater than the unmasked detector amplitude to validate a particle’s acceptance. Instead of comparing signal voltages with the annulus, like the FSSP-100, the FSSP-300 works on the principle of optical particle imaging. Optical particle imaging is established from the collected light that passes through a polarizing beam splitter rotated at 45° with respect to the plane of polarization to provide a 50/50 split with the transmitted light imaged onto a masked photodetector (Baumgardner, 1992).

Part II. Sizing Calibrations

The particle size can be predicted from the measured light intensity using Mie scattering theory with the knowledge of the wavelength of incident light, particle index of refraction and the scattering angles over which the light is collected. The voltage of the signal is converted to a particle size using a 15 channel pulse height analyzer (PHA) whose comparator levels are preset corresponding to certain size intervals. PMS uses a set level for their sizing intervals by approximating a smooth curve that goes through the theoretical scattering cross section values calculated from the Mie scattering theory. By assigning a scattering cross section to each interval by using calibration data, particles of different sizes can be separated and placed within their respective intervals. One

interesting effect that occurs is that Mie scattering theory predicts a multivalued function such that particles of several sizes can scatter the same amount of light. From Mie theory for a polarized plane wave having wave number, k , incident on a sphere with radius, r , the scattering cross-section (in cm^2 per particle) for radiation scattered into a solid angle having axial symmetry with respect to the direction of the light source is:

$$R = \frac{\pi}{k^2} \int_{\Omega} \left\{ |S_1|^2 + |S_2|^2 \right\} \sin \theta d\theta \quad (\text{A1.2.1})$$

where $S_1(x, n, \theta)$ and $S_2(x, n, \theta)$ are the Mie scattering amplitude functions corresponding to light polarized with electric vector perpendicular and parallel to the plane of scattering (Pinnick and Auvermann, 1979). They depend on the particle size parameter $x = rk$, the refractive index n , and the scattering angle θ . The angular integration is over the solid angle Ω subtended by the light-collecting optics. Figure A1.2.1 and Figure A1.2.2 display the theoretical response as a function of diameter and refractive index for a wavelength of 638 nm. Multivalued regions begin to occur for $D_p > 1.0 \mu\text{m}$. Pinnick *et al.* (1981) suggested redefining channel limits and combining channels to remove the ambiguity in sizing. Table A1.2.1 from Cerni and Cooper (1982) gives an example of the PHA levels and their corresponding diameters for glass beads with the same refractive index as water. The column labeled PMS refers to the manufacturer calibrations, while the smoothed Mie column represents the diameters derived by employing a single-value approximation. The Mie column is the exact Mie scattering curve for water. In order to eliminate some ambiguity in sizing for this study, a cubic spline equation was used to average scattering cross sections per channel interval (via personal communication with Dr. Darrel Baumgardner).

Cerni (1983) also studied the effect of air speed on sizing in laboratory experiments in which glass beads were accelerated past the sampling area at different airspeeds. He used the counts from the velocity averaging circuitry to determine the speed of beads passing through the sample area. Air speed variations introduce some uncertainty (probably less than 10%), based on the results of Cerni (1983).

Part III. Flow distortions

Norment (1988) calculated flow-induced distortions of water drop flux and speed. This research explored the effects of mounting the FSSP on the wing tip of a Twin Otter airplane. Three-dimensional simulations were developed in order to determine how the airflow would be affected around the instruments, and how the angle of attack would affect sampling of particles due to flow distortions. Norment (1988) found that the structure of the support arm-measurement tube combination presented a considerable obstacle to the flow. 90% of the concentration would not be influenced by flow distortions around the instrument at 0° attack angle. However, for an attack angle of 4°, only 77% of the concentration was found to be unaffected. Flow distortions and angles of attack were not factored into the concentration calculations used in this work, introducing some uncertainty to the reported concentrations. Using the true air speed (*TAS*) instead of the actual wind speed, which is affected by putting the instruments in the flow and the angles of attack, would underestimate the measurement of particle counts, hence underestimating the derived concentrations by ~ 10 – 25 %.

Part IV. Concentration corrections

ACE-1 data were taken from the raw instrument counts for a sampling rate of 1 Hz. The accuracy of measuring the particle concentrations depends upon an accurate measurement of the FSSP sampling volume, as well as on the detection of all particles within that volume (Dye and Baumgardner, 1984). The FSSP-300 concentrations are determined by

$$N_{300} = \frac{n_{300}}{(TAS)(0.05)} \quad (A1.4.1)$$

where N_{300} is the concentration for the FSSP-300, n_{300} is the number of counts, TAS (m s^{-1}) is the true airspeed, and 0.05 mm^2 is the sampling area. The FSSP-300 computed sampling area (0.05 mm^2) takes into account the depth-of-field, geometry, electronic measurements, and the beam diameter. The concentration correction used for the FSSP-100 has the form

$$N_{100} = \frac{n_{100}}{(0.60)(BD)(DOF)(TAS)} \quad (A1.4.2)$$

where N_{100} is the concentration, n_{100} is the number of counts, 0.6 is the effective beam diameter, BD ($= 0.19 \text{ mm}$) is the total beam diameter, and DOF ($= 2.56 \text{ mm}$) is depth-of-field area.

Part V. Concentration and sizing uncertainties

The accuracy of measuring particle concentrations was limited by uncertainties in the optical sample volume and by detection errors caused by coincidence and deadtime

losses and poor sampling (Baumgardner, 1983; Baumgardner et al., 1989; Baumgardner et al., 1992). The depth-of-field can vary up to 10% in error, and variations in the beam diameter can produce an error of approximately 10%. Beam fraction variations range from 40 – 100%. Activity losses, which is any particles entering the sampling volume that are ignored by the electronics, are also important, with variations ranging from 10 – 100%. The “root-sum-square” (RSS) of these uncertainties leads to an expected uncertainty of ~ 20% in concentrations for the FSSP-300 and FSSP-100. The sizing uncertainties are due to laser inhomogeneity (10%), electronic response time and coincident particles (10%), and calibrations for scattering intensities (10%). The RSS of these uncertainties in accuracy was ~ 15%.

Part VI. Lower Detection Limit (*LDL*) approximation

The *LDL* was determined by looking at three different time segments displaying low number concentrations, which would possibly be linked to instrument noise. Figure A1.5.1 displays an example of low number concentrations for N_I , used to establish the lower detection limit. The same procedure was done for the surface area concentrations, volume concentrations, and total light scattering coefficient. The surface area and volume concentrations were more sensitive because the *LDL* would be a function of the size of the shape of the number distribution. After looking at three different time segments from various flights it was found that the *LDL* had consistent values. The same time segments were used to determine the *LDL* for the total light scattering coefficient since they are a function of surface area concentrations.

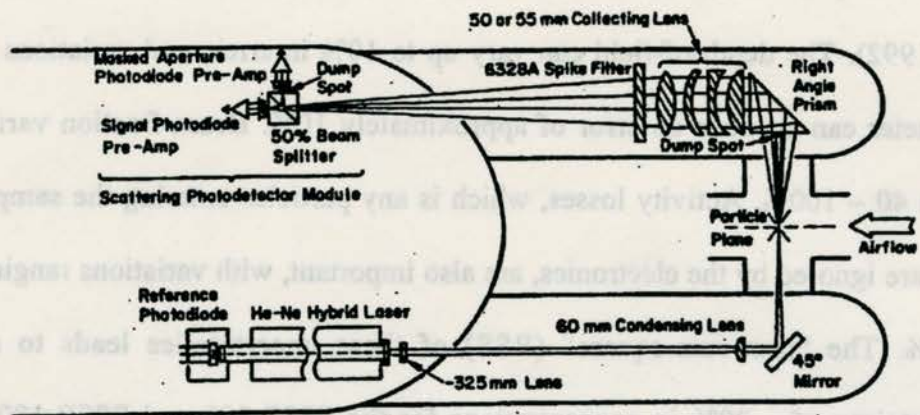


Figure A1.1.1 A schematic showing the optical path and components in the FSSP-100 (reproduced without permission from Dye and Baumgardner, 1984).

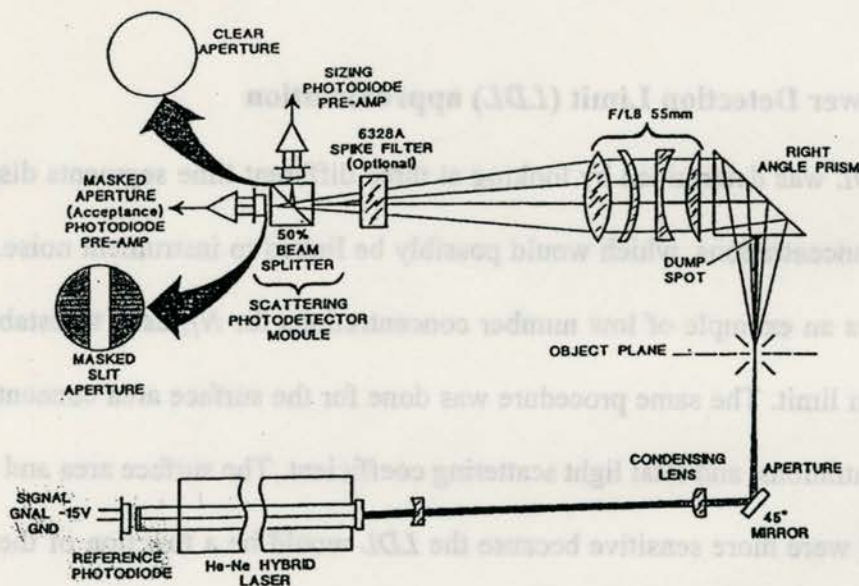


Figure A1.1.2 A schematic showing the optical path of the FSSP-300 (reproduced without permission from Baumgardner, 1992).

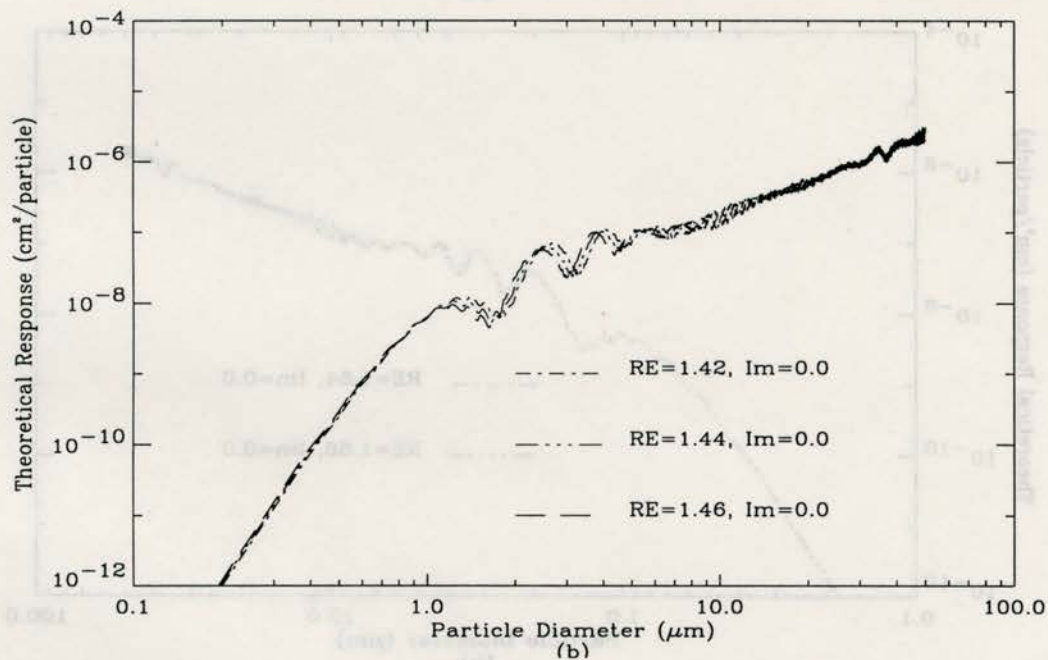
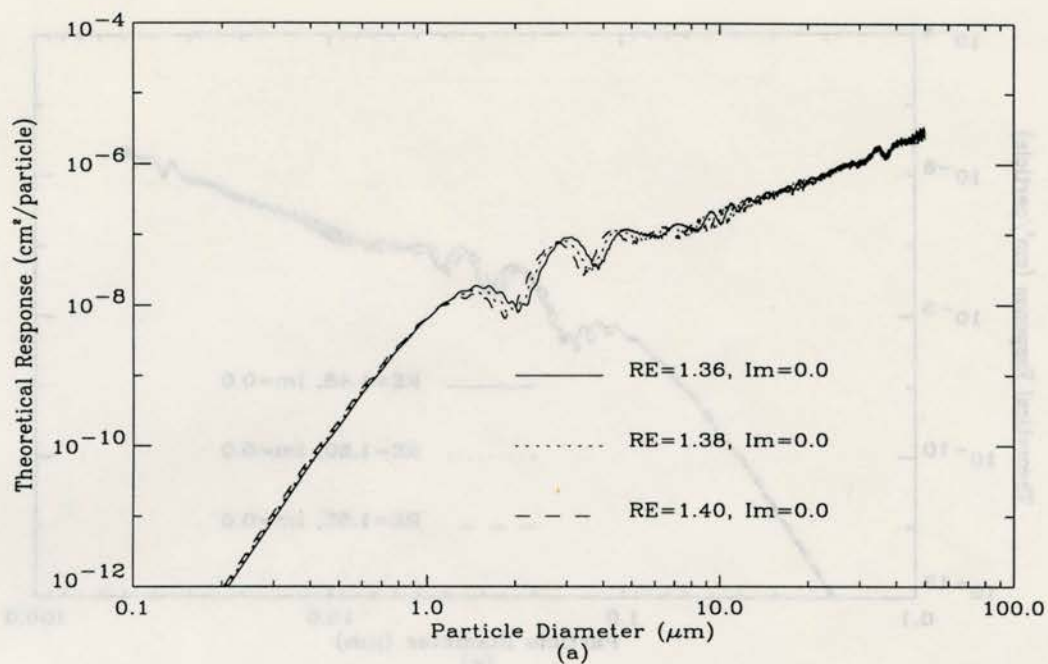


Figure A1.2.1 Theoretical response (cm²/particle) as a function refractive index. Part (a) displays the theoretical response function for 1.36, 1.38, and 1.40. Part (b) displays the theoretical response function for 1.42, 1.44, and 1.46. Im represents the absorption of the particle.

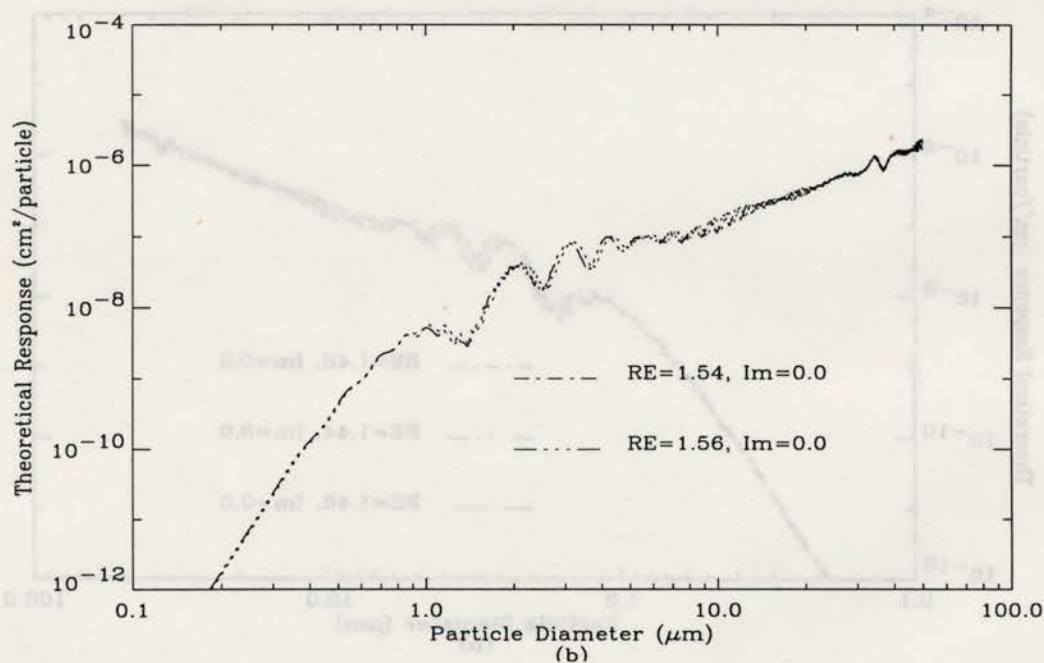
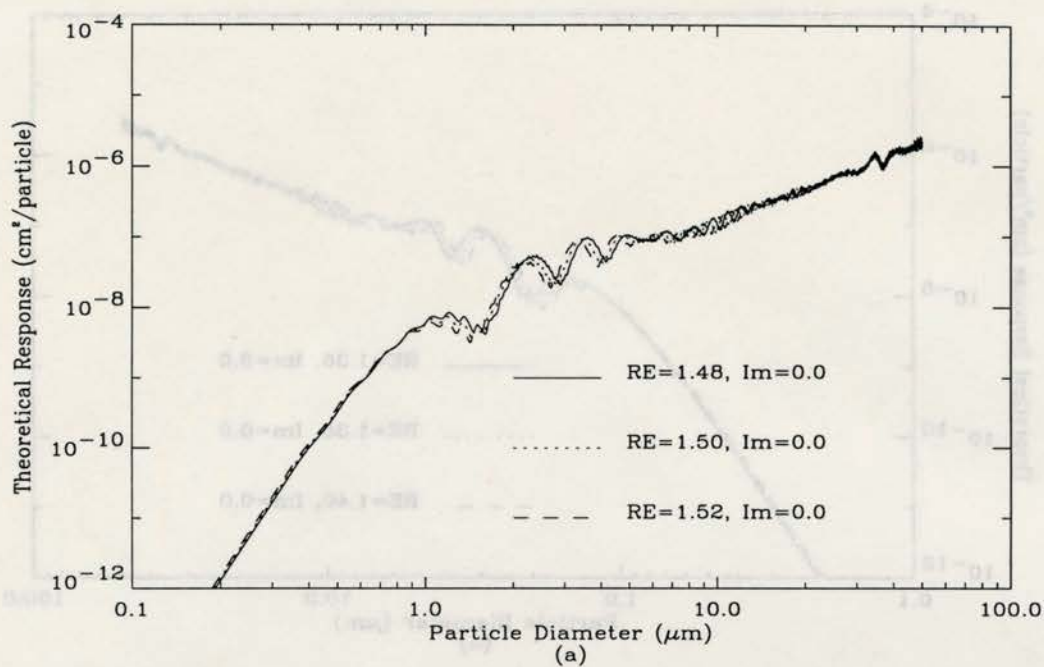


Figure A1.2.2 Theoretical response (cm²/particle) as a function refractive index. Part (a) displays the theoretical response function for 1.48, 1.50, and 1.52. Part (b) displays the theoretical response function for 1.54, and 1.56. Im represents the absorption of the particle.

Table A1.2.1 FSSP-100 Calibration (Cerni and Cooper, 1982)

PHA level	Range 0		
	PMS	Smoothed Mie	Mie
1	2.0	1.9	—
2	5.0	4.3	—
3	8.0	6.5	7.6
4	11.0	8.8	9.6
5	14.0	11.1	11.2
6	17.0	13.4	13.6
7	20.0	16.5	—
8	23.0	19.1	18.2
9	26.0	22.5	23.0
10	29.0	25.7	25.5
11	32.0	29.0	28.6
12	35.0	32.2	31.5
13	38.0	35.2	35.1
14	41.0	38.0	38.1
15	44.0	41.1	41.6
16	47.0	43.3	43.5

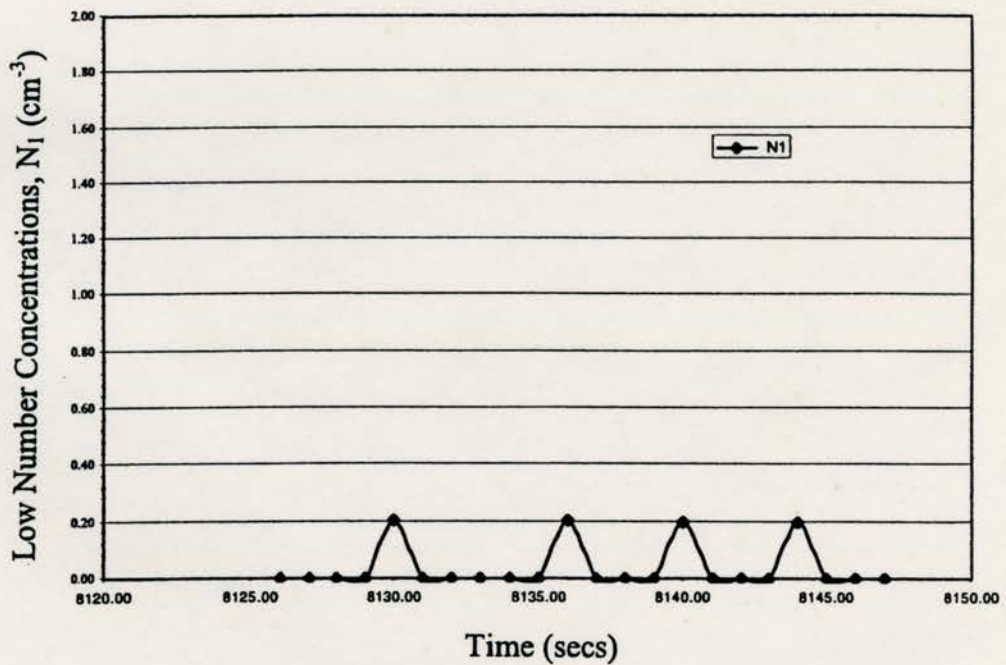


Figure A1.6.1 Low number concentrations (N_1) as a function of time. These concentrations were used to derive the *LDL*.